Journal Pre-proof

In-situ tensile-shear test in SEM and DIC analysis of two pearlitic steel microstructures: undeformed-coarse and deformed-refined

Pablo B. Paiva Leão, João R. Barros Neto, Samuel Filgueiras Rodrigues, João Victor B. Xavier, Jorge Luiz Cardoso, Luis Flavio Gaspar Herculano, Tiago Nunes Lima, Antonio J. Ramirez, Hamilton Ferreira G. de Abreu

PII: S2238-7854(23)01117-1

DOI: https://doi.org/10.1016/j.jmrt.2023.05.154

Reference: JMRTEC 7399

To appear in: *Journal of Materials Research and Technology*

Received Date: 27 March 2023

Revised Date: 15 May 2023

Accepted Date: 16 May 2023

Please cite this article as: Paiva Leão PB, Barros Neto JR, Rodrigues SF, Xavier JVB, Cardoso JL, Gaspar Herculano LF, Lima TN, Ramirez AJ, de Abreu HFG, In-situ tensile-shear test in SEM and DIC analysis of two pearlitic steel microstructures: undeformed-coarse and deformed-refined, *Journal of Materials Research and Technology*, https://doi.org/10.1016/j.jmrt.2023.05.154.

In-situ tensile-shear test in SEM and DIC analysis of two pearlitic steel microstructures: undeformed-coarse and deformed-refined

Pablo B. Paiva Leão [a,b], João R. Barros Neto [c], Samuel Filgueiras Rodrigues [a,d,*], João Victor B. Xavier [a], Jorge Luiz Cardoso [a], Luis Flavio Gaspar Herculano [a], Tiago Nunes Lima [b], Antonio J. Ramirez [e], Hamilton Ferreira G. de Abreu [a]

[a] Materials Characterization Laboratory (LACAM), Department of Metallurgical and Materials Engineering, Federal University of Ceará, Campus do Pici, Bloco 729, Fortaleza 60020-181, Ceará, Brazil

[b] SENAI CIMATEC, SENAI Innovation Institute for Conformation and Joining Materials (ISI-C&UM), Orlando Gomes, 1845, 41650-010, Bahia, Brazil

[c] Department of Materials Engineering, Federal University of Piaui, Technology Center, Federal University of Piauí (UFPI), Teresina 64049-550, PI, Brazil

[d] Graduate Program in Materials Engineering, Federal Institute of Education, Science and Technology of Maranhao, Sao Luis, Maranhao, 65030-005, Brazil

[e] Department of Materials Science and Engineering, The Ohio State University, Fontana Laboratories Suite 2136 140 W. 19th Avenue, Columbus, Ohio, USA

Abstract

The deformation and fracture behaviors of undeformed-coarse (UC) and deformed-refined (DR) pearlitic steel microstructure were investigated via in-situ tensile-shear (TS) test in scanning electron microscopy (SEM). An original TS sample geometry was designed. Secondary Electron (SE) images were recorded in real-time and digital image correlation technique was applied to them. Due to the DR's refined microstructure, SE images, backscatter electron images, and electron backscatter diffraction techniques were additionally employed in the DR condition under an interrupted TS test. The results showed that the DR pearlitic microstructure presented a higher shear strength and absorbed energy, compared to UC, during the TS performance. UC's pearlitic microstructure experienced a high degree of microstructural deformation, while DR seemed to be highly rigid. Strain concentration was mainly observed in the UC's colony boundaries, in the DR's GBs-α, and in the DR's colony with lamellae parallel to the tensile direction. The decohesion phenomenon was observed at colony boundaries and ferrite/cementite interfaces, respectively, for UC and DR specimens. These decohesion phenomena were related to crack nucleation in both pearlitic microstructure conditions. Finally, the shear rupture occurred abruptly for UC and slowly for DR, resulting in fractures mainly comprised of a sheared flat surface and dimples, respectively.

Keywords: Pearlite, In-situ, Shear-tensile, DIC, Fracture, Deformation.

* Corresponding author: samuel.filgueiras@ifma.edu.br

1. Introduction

Pearlitic steel wires are used in a wide range of engineering applications, such as tire cords, springs, suspension bridge cables, etc. The excellent balance of strength, torsional ductility, and formability make pearlitic steel suitable for wire-related employment [1-4]. In this way, the pearlitic microstructure can be classified by subsets known as blocks (or nodules) and colonies.

Categorically, the prior austenitic grain integrates many blocks, and an individual block comprises a few pearlitic colonies. Specifically, a block is a zone determined by an identical ferritic crystallographic orientation. While a lamellar colony, constituted of succeeding lamellae of cementite and ferrite, is defined as a region comprised of cementite lamellae orientated in the same direction [5,6]. In general, the mechanical properties of pearlitic steel are regulated by its microstructural parameters that include prior austenitic grain size, interlamellar spacing (IS), spatial arrangement of cementite lamellae, cementite structure, block size, etc. Moreover, boundaries of block and colony are regularly mentioned as significant structures during the evaluation of strain distribution in pearlitic microstructures [1-6].

In this context, the literature has pointed out [7,8] that the prior austenitic grain size significantly influences ductility and toughness in pearlitic steels. Additionally, Zhou et al. [7] concluded that the dominant substructure that affects the toughness of pearlitic steels is the pearlitic block size due to its control of the cleavage facet size. These authors also reported that there is a proportional relationship between the sizes of the prior austenitic grains and pearlitic blocks. Moreover, the IS has straight dominance in the strength of pearlitic steels due to the restriction of the dislocation mean free path [9]. However, Hyzak et al. [10] demonstrated that pearlite colony size has a minor effect on cleavage crack propagation. On the other hand, different geometrical setups of pearlite cementite lamellae about the tensile axis can result in inhomogeneous strain throughout the pearlitic microstructure related to crack initiation. More specifically, heterogeneous strain is commonly associated with divergences in the ferritic slip plans' direction and cementite lamellae's spatial orientation. In this regard, the softer ferrite lamellae undergo earlier yielding compared to the hard cementite plates. This heterogeneous deformation behavior can develop pile-ups of dislocations and stress concentration at the ferrite/cementite [2,5]. For example, Teshima et al. [5] found a greater local strain in ferrites from colonies with cementite lamellae aligned at 45° about the tensile axis due to its free dislocation motion. In contrast, they noticed cracks initiating in colonies arranged at 90° about the tensile axis. Furthermore, a similar result was found by Durgaprasad et al. [2]. They observed a maximum shear strain in lamellar ferrites of colonies with their cementite lamellae fitted at 45° about the drawing axis. From a macro viewpoint, the lamellar alignment of the colonies can also impact the total shear strain to the failure of a steel wire under torsion. For instance, Durgaprasad et al. [11] reported that the increase in the number of colonies with lamellae aligned in the range of 60 - 90° about the wire axis reduces the total shear strain to failure. In this regard, shear bands are prone to be developed due to the non-homogeneous strain distribution in pearlitic colonies [12,13]. In addition to this, block size and alignment of the colony lamellae can determine the failure mode of the component [5,14,15].

Likewise, the cementite lamellae have also their specific role during the deformation of pearlitic microstructures. Tagashira et al. [13] suggested that the slip mechanism during pearlite deformation can start in ferrite and continue into the cementite lamellae. They also indicated that multiple slip systems might operate in cementite to preserve the compatibility between ferrite/cementite structures. However, it has been pointed out by some investigations [5,13] that the cementite lamellae fracture takes place, once the preferential slip plans of both, cementite and ferrite, are not in cooperation. In view of this, the main slip plan's families available in the ferrite (α) and cementite (θ) phases are $\{110\}_{\alpha}$, $\{112\}_{\alpha}$, $\{123\}_{\alpha}$,$\{100\}_{\theta}$, $\{010\}_{\theta}$, $\{001\}_{\theta}$, $\{110\}_{\theta}$, and $\{210\}_{\theta}$ [16,17]. In addition, Zhou et al. [4] noted that cold-deformed cementite lamellae are dominantly composed of an amorphous phase lattice structure. The authors also indicate a possible absorption of dislocations by the amorphous cementite lamellae which can reduce strain and stress concentrations at the ferrite/cementite interface. Otherwise, the

author reported that cementite lamellae consist mainly of nanocrystalline grains after some thermal treatments acted like barriers against dislocation movement, which can promote stress accumulation. Regarding the aforementioned microstructural heterogeneity behaviors, SEM images together with the digital image correlation (DIC) technique are powerful tools widely used to detect inhomogeneous strains throughout microstructures under deformation [18, 19, 20].

In addition to tensile efforts, pearlitic steel wires must maintain a suitable level of shear resistance during their wire-related applications [21]. Therefore, torsion tests are extensively used to measure the shear strength and strain of pearlitic wires [4,21,22]. However, it is pretty difficult to assess the behavior of pearlite colonies during the progress of torsion tests due to the gradient of shear components along the circumferential direction of the wire [3]. For instance, Guo et al. [1] proved the establishment of a non-uniform shear strain variation in the radial wire section as a result of the specimen geometry during the torsion test. In detail, they observed a heterogenous behavior of microtexture near the external wire surface and macro texture throughout the entire radial length. With this particular context, the failure mechanisms related to the pearlitic microstructure are usually estimated due to the difficulties associated with the regular torsion test. To overcome these obstacles, the present research brings a novelty manner to evaluating the behavior of pearlites under shear deformation via a tensile-shear (TS) test. The TS test can provide a more stable shear state and easier access to the pearlite surface under shear. This experiment was conducted via in-situ observations in scanning electron microscopy (SEM) in cooperation with the DIC technique. Under this scope was possible to verify the strain heterogeneities and the exact instant that two types of pearlitic steel microstructure (undeformed-coarse and deformed-refined) start to fail under shear deformation. validate

2. Materials and methods

2.1 Samples processing

Commercial SAE 1075 pearlitic steel was used in this study. The chemical composition of the as-received steel is available in **Table 1** and it was lab-processed targeting two conditions of pearlitic microstructure: undeformed-coarse (UC) and deformed-refined (DR). In this regard, the UC microstructure was achieved by applying in the starting sample (thickness 8 mm x length 40 mm x width 50 mm) a thermal treatment performed at 850 °C for 300 s followed by a slow cooling rate of 1 °C/min up to room temperature in an Argon gas-controlled atmosphere tube furnace. This thermal treatment is focused on producing a microstructure with fewer defects, which means a raw condition. A representative diagram of UC's thermal treatment is exhibited in **Figure 1 (a)**. On the other hand, the DR condition was obtained through five lab-simulated processes based on the actual manufacture of rectangular wires for tensile armor application in flexible pipelines [23]. This lab-process route is illustrated in **Figure 1 (b)**. In this context, the starting sample underwent 45% hot-rolled reduction in multiple passes (≈0.6 mm of reduction/pass and finish rolling temperature of ≈906 °C). After hot rolling, the steel was austenitized at 950 °C for 390 s, and then, quenched into a bath salt at 550 °C for 40 s (patenting treatment). Subsequently, 65% cold-rolling reduction (≈0.1 mm in thickness reduction/pass) was introduced in the patented specimen, followed by a short time (60 s) stress-relief treatment at 400 °C. Both rolling processes were executed by using a laboratory scale rolling machine with diameter rolls of 110 mm and a rolling speed of 8m/min. Next, the stress-relieved sample was cut in a rectangular dimension of 1.54 mm (thickness) x 12.5 mm (width) x 60 mm (length). In this case, the rolling and length directions are parallels. Finally, the DR condition was obtained after the application of four consecutive three-point bending steps alternating the superior and

inferior surfaces of the stress-relieved sample. This procedure simulates the operation of re-winding wire into coils [24]. A universal testing machine (landmark 370.10) with a maximum load of 100kN was used to carry out the bending experiments. Pins with a roller's diameter of 10 mm, a distance of 40 mm between the support pins, a displacement rate of 2 mm/min, and 4.5 mm as the maximum displacement of the loading pin were the parameters adopted during the three-point bending test. After that, the UC and DR tensile-shear (TS) specimens were obtained using an electro-discharge machine. The geometry and dimensions of the TS specimen are provided in **Figures 2 (a)**, **(b)**, and **(c)**.

Moreover, there is one more operation for building the tensile armor layer, the wire wrapping process. This process consists of twisting the prior deformed rectangular wires into a helical shape around the pipe [24]. Consequently, the wires experience an additional plastic deformation with a certain degree of shear in this torsion procedure. Based on this, the evaluation of the DR microstructural setting, under the in-situ TS experiment in SEM, can provide relevant insights into the performance of a realistic manufactured pearlitic steel state taking into account the twisting process. Otherwise, the coarse UC microstructure is a valuable hypothetical condition that was designed to assess the behavior of a raw pearlitic microstructure (unprocessed) under shear circumstances. In this context, the comparison of both pearlitic steel scenarios is fundamental to understanding the influence of the microstructural features on their preferable sites for strain accumulation and deformation heterogeneities during the TS mechanical loading. This can help to optimize and design the investigated class of steel with superior mechanical properties.

2.2 In-situ tensile-shear (TS) experiment, digital image correlation (DIC), and microhardness

For in-situ observations, the specimens were grounded (using sandpapers from #240 to #2000 grit), polished (using diamond suspensions of 6, 3, and 1 µm), and etched with 4% nital solution. The in-situ procedure was performed using a kammrath-weiss tensile stage with a maximum loading of 5kN, as shown in **Figure 2 (d)**. During the in-situ experiment, a constant displacement of 0.1 µm/s was established and secondary electron (SE) image acquisition was carried out in real-time in a resolution of 1536 x 1024 pixels using a THERMO SCIENTIFIC QUATTRO field emission gun (FEG) scanning electron microscope (SEM). The SE images were captured employing an accelerating voltage of 5 kV, a current of 0.18 nA, and a working distance (WD) of 20 mm. The high WD was implemented in this experiment because of safety measures due to the complex dimensional setup of the tensile stage in the SEM chamber (see **Figure 2 (e)**). After the specimen's failure, QUATTRO FEG-SEM was also employed for obtaining fractographic SE images using an accelerating voltage of 20 kV, a current of 3.2 nA, and a WD of 8.5 mm. Additionally, the open source 2D-DIC MATLAB software (Ncorr v1.2) was adopted to compute the *u*-displacement component (into the x-axis) and the Eulerian shear strain (e_{xy}) among the recorded images during the in-situ TS experiment. A subset size of 55 pixels and a subset space of 1 pixel were chosen for the DIC proceeding. Finally, microhardness measurements were carried out by using a Leco AMH43 automatic machine setting a load of 200 gf and a holding time of 10 seconds. This procedure was conducted by inserting twenty indentations per sample with a spacing of 180 microns between them.

2.3 Interrupted tensile-shear (TS) experiment in the RD specimen

A THERMO SCIENTIFIC APREO FEG-SEM was adopted to perform electron backscatter diffraction (EBSD) analyses, SE image, and backscattered electrons (BSE) image acquisitions just before and after the interrupted TS test using the same aforementioned tensile stage apparatus. In this case, the TS procedure was performed outside the SEM chamber and it was terminated immediately after the moment when an abrupt load drop started to occur after 200 µm of elongation (using the already obtained RD's in-situ elongation-load curve as reference). The APREO FEG-SEM was coupled with an EDAX EBSD detector and BSE detectors placed inside the

microscope column. The EBSD analyses were conducted with an operating voltage of 20 kV, a step size of 50 nm, a WD of 8 mm, and a sample tilt angle of 70°. In this operation, the SE images and the BSE images were implemented using, respectively, an accelerating voltage of 20 kV and 5 kV, a current of 6.4 nA and 1.6 nA, and a WD of 8 mm and 1.5 mm. For EBSD, SE, and BSE image acquisition during the interrupted investigation, the specimen also received the regular metallographic preparation with an additional vibratory polishing (with 0.04 μm colloidal silica), and no etch was applied. Finally, the EBSD data were evaluated through OIM and MTEX software, and their inverse figure pole (IPF) maps were plotted in the z-direction.

3. Results and discussion

3.1 Initial microstructural characteristics of pearlitic steel before the tensile-shear (TS) experiment

This topic aims to detail the microstructural differences between the initial condition of UC and DR specimens. The start microstructures are presented in **Figures 3 (a)** (UC) and **(b)** (DR). In this regard, UC reveals the coarsest pearlitic interlamellar space (IS) (402.6 ± 64.4 nm) and colony size (16.0 ± 3.9 μm) in comparison to the DR's pearlitic microstructure condition (IS = 173.2 ± 37.6 nm and colony size = 9.9 ± 1.6 μm). Based on this, the IS is controlled by the temperature of the austenite-to-pearlite transformation which is a diffusion-controlled reaction [25]. Otherwise, the size of pearlitic colonies and blocks depends on the prior austenitic grain size because the austenitic grain boundaries are sites for pearlite nucleation [25]. In this way, the slow cooling in the thermal treatment (**Figure 1(a)**) used to produce the UC microstructure increases this sample's holding time under austenitization temperatures. As a consequence, the UC's prior austenitic grain can significantly grow letting UC prone to produce coarse pearlitic colonies and blocks. Also, this slower cooling rate allows the austenite-to-pearlite transformation to occur in UC at a high temperature developing pearlites with thicker IS. Conversely, the faster cooling applied in DR via the patenting treatment (**Figure 1(b)**) can result in the opposite microstructural effect. After patenting treatment, DR additionally underwent 65% cold-rolling reduction that can also enhance the IS refinement [23]. Another point is that the volume fraction of grain boundaries ferrite (GBs-α) found in UC (5.6%) and RD (4.3%) were not identical. In this context, it is expected that DR has the highest volume fraction of GB-α due to its inferior prior austenitic grain size and higher cooling rate after austenitization (inhibits manganese partitioning) [26]. However, this contradiction was assumed to be a consequence of the distinct states and morphologies of the GBs-α in both studied conditions that can intervene in the phase quantification process. For instance, GBs-α in the UC specimen exhibit an almost polygonal shape and they are not deformed, while they are in a pancake-like shape and stretched around the rolling direction in the DR condition. Also, **Figure 3 (i)** displays the morphological angle distribution of cementite lamellae in pearlites about the tensile axis for both studied specimens. In view of this, the greater number fraction of the morphological angle in the DR condition is mainly concentrated in the range from 0° to 10° and it tends to decrease as the angle increases. It means that most of the pearlite colonies in DR are closely aligned to the tensile axis due to the prior cold rolling deformation [13]. Otherwise, the UC's pearlite colonies seem to be randomly orientated about the tensile axis.

Moreover, **Figures 3 (c)** (UC) and **(f)** (DR) present the inverse figure pole (IPF) maps of the two evaluated specimens in their initial states. In addition, the accumulation of local plastic strain in the steel matrix can be investigated through kernel average misorientation (KAM) and distribution of low-angle grain boundaries (LABs) as well as medium-angle grain boundaries

(MABs) [27]. Specifically, KAM is the relative average misorientation between a given point and its nearest neighbors inside the same grain [27]. **Figures 3 (d)** (UC) and **(g)** (DR) depict the KAM distribution maps obtained from both IPF maps and their kernel values are summarized in **Figure 3 (j)**. It is possible to note that the UC`s KAM map is mainly constituted of blue regions in low kernel values. Also, there are some intermediary KAM intensities in UC, in green lines, that seem to be around the pearlitic colony boundaries. Otherwise, the KAM distribution map for DR displays essentially areas with intermediary values of KAM (in green color) including some red color regions meaning higher KAM intensities (≈5°). In this context, the overall average of KAM was 0.6° ± 0.4 for UC and 2.1° ± 1.1 for DR. Furthermore, regarding grain boundary distribution, **Figures 3 (e)** (UC) and **(h)** (DR) show maps with the distribution of the grain boundary types, and **Figure 3 (k)** reports their density normalized in length per area. The LABs and MABs (misorientation <15°) indicate areas with a concentration of geometrically necessary dislocations (GNDs) [28]. In this way, the densities of LABs (2° ~ 5°) and MABs (5° ~ 15°) in UC were respectively 0.03 μm/μm² and 0.02 μm/μm², which are almost null values. Unlike, DR has a higher density of LABs (2.92 μm/μm²) and MABs (1.51 μm/μm²) in its ferritic matrix. Therefore, the evaluation of KAM and grain boundary distributions confirm that DR is initially plastic-deformed while UC is not. Additionally, a great divergence of HABs' density was found between UC (0.10 μm/μm²) and DR (0.93 μm/μm²). The HABs are usually related to the pearlitic block boundaries in pearlitic steels [7,25]. In this context, although it was not possible to measure the pearlitic block size due to the small EBSD areas, it can be qualitatively said that the pearlitic block size should be larger in UC than in DR. This outcome is also expected based on the aforementioned effect of the different cooling rates on both specimens' microstructures. All the microstructural features obtained from both initial states are summarized in **Table 2**.

3.2 In-situ tensile-shear (TS) experiments and digital image correlation (DIC)

This section centers attention on describing the mechanical and microstructural behavior of pearlitic steel during the in-situ TS experiment. In this regard, **Figure 4** provides the elongation-load curves obtained from the TS tests performed in the UC and DR pearlitic steel states. The structural properties extracted from each elongation-load curve and the microhardness average of UC and DR are available in **Table 3**. Based on this, it is worth noting that DR has shorter ultimate elongation and higher values of elastic stiffness, ultimate load, and absorbed energy in comparison to UC. These structural properties indicate that DR holds higher resistance to elongate. This mechanical behavior can be attributed to the DR's microstructural features, such as its thinner IS, cementite lamellae closely aligned to the tensile axis, plastic-deformed ferritic matrix, and smaller pearlitic blocks. More specifically, the refined IS can restrain more effectively the movement of dislocations because they have shorter free paths and more cementite lamellae acting as barriers [9,29]. Moreover, Teshima et al. [5] reported that plastic deformation can be efficiently restricted when the lamellae are aligned parallel or perpendicular to the tensile axis due to pile-ups of dislocation at the ferrite/cementite interface. Conversely, some authors [2,5] have reported that dislocation can move freely in pearlite with cementite lamellae aligned around 45° about the tensile axis. In this context, there are significant pearlitic colonies arranged in a hard set for plastic deformation in DR condition which may also contribute to its higher strength to elongate. Furthermore, the introduction of prior plastic deformation in DR develops a work-hardened state where some slip plans and ferrite/cementite interfaces can be initially saturated with dislocations that hinders the further dislocations' motion. In this case, slips can occur again when a superior critical load is achieved, which explains why the load-elongation curve of RD has a significant elastic region and no-strain hardening behavior. Unlike, UC exhibits a small elastic region and a considerable strain hardening zone followed by a brief necking, just

before the rupture. Furthermore, that divergence in the ability to resist deformation can also explain the difference in microhardness found in the DR (409 ± 7.9 HV) and UC (223.1 ± 11.2 HV) specimens. Moreover, it is pointed out by the literature [7,30] that pearlitic block size has a significant influence on the toughness of pearlitic steels. Therefore, the highest amount of absorbed energy during the DR's TS test can be a result of its assumed smaller pearlitic block size. Finally, the structural properties discussed above suggest that DR presents advantageous engineering attributes for wire-related applications in analogy to the UC pearlitic condition.

In addition, the x-marks in **Figure 4** indicate where the in-situ SEM observations were selected for demonstrating the progress of microstructural modifications under TS deformation. In this case, each of the two elongation-load curves has its own x-mark distribution due to their distinct mechanical behavior. The chosen regions were: original state (1UC and 1DR), strain hardening (2UC and 3UC), necking (4UC, 2DR, 3DR, and 4DR), and failure (5UC and 5DR). Regarding the elastic zones, the original microstructures did not undergo any significant modifications in both studied cases. **Figures 5** and **6** show the macro view of plastic deformation evolution for, respectively, UC and RD following their x-mark positions in **Figure 4**. In general, it is possible to observe a left-hand rotation as an effect of the shear proceeding. Also, this event was confirmed by the measurement of the *u*-displacement component, which was obtained via the DIC technique (see **Figures 5 (f)** and **6 (f)**) from both original states (1UC and 1DR) up to the necking stages (4UC and 4DR). In view of this, the top regions slide into the right sides, while the bottom areas move into the left laterals, and between them, there are also zones with zero *u*-displacement meaning that the in-situ investigations were performed in the geometrical middle between the shear components. However, the *u*-displacement values are incomparable between UC and DR because the images from each condition in **Figures 5** and **6** have different magnifications that interfere with the total displacement on each of those specific evaluated regions. Moreover, the central regions of **Figures 5 (a)(b)(d)(e)** and **6 (a)(b)(d)(e)** marked with a red dashed rectangle are presented in higher magnification, respectively, in **Figures 7** and **8** including their Eulerian shear strain (e_{xy}) maps. In this regard, the maximum shear strain value in each map is negative and represented by dark blue color because the 2D DIC code implemented in this work considers the positive reference of the Y axis going down, which means below zero, while its negative reference is set up in the opposite direction that implies above zero, as illustrated in **Figures 5 (f)** and **6 (f)**.

Concerning UC, it is pointed out by yellow arrows in **Figures 5 (a)**, **7 (a)**, and **7 (b)** (original state) some pearlitic lamellae with cementite broken. It demonstrates how brittle is the thick cementite even under no loading application. Then in the hardening strain zone, it can be seen that the microstructure in 2UC (**Figures 5 (b)**, **6 (d)**, and **6 (e)**) underwent a slight rotation, and a small heterogeneous strain (maximum e_{xy} of -0.08) started to be concentrated at the pearlitic colony boundary as displayed in the dark blue area of **Figure 6 (f)**. Subsequently, in 3CU (**Figures 5 (d)**, **6 (g)**, and **6 (h)**), the rotation increased together with a microstructural stretching into ≈53.7° about the shear direction. At the same time, many lamellae of cementite started to break as indicated by yellow arrows in **Figure 6 (h)**, while the maximum shear strained region reached a value of -0.7 and expanded from the pearlitic colony boundary throughout a low resistance area within a colony constituted of non-continuous cementite (see **Figure 6 (i)**). Also, intermediary strained regions in yellow color (≈ -0.3) considered unstable regions (comprised of pearlitic colony boundary, coarse cementite, or broken cementite lamellae) were found in **Figure 6 (i)**. It is worth mentioning that the coarse pearlitic region indicated by the white arrow in **Figure 6 (i)** seems to cooperate with the instability and fracture of the nearby cementite lamellae. Next, the necking stage (4UC), in **Figures 5 (e)**, **7 (j)**, and **7 (k)**, reveals that the rotation

and microstructural stretch became sharper resulting in pearlitic colonies and GBs-α elongated into ≈ 40° about the shear direction. This event can be a consequence of the combined effect of the principal stress components caused by the process of shear, as illustrated in **Figure 5 (c)** [31]. Additionally, decohesion between pearlitic colonies was identified in 4UC as indicated by yellow arrows in **Figures 7 (j)** and **7 (k)**. Moreover, it can be realized in **Figure 7 (l)** that the high-strained regions were still at the pearlitic colony boundaries followed by the unstable zones within the colonies. In this case, the maximum e_{xy} intensified to -2.5. In addition, a huge deformed region was observed just before the sample fails (see **Figure 5 (g)**). Finally, the rupture in the UC specimen (5UC) occurred abruptly with a fracture almost perpendicular to the stretching direction as shown in **Figures 5 (i)** and **5 (j)**. This instantaneous break caused a fuzzy image in **Figure 5 (i)** due to the fast motion of the specimen. The quick UC's fracture can be likely related to its assumed big pearlitic block size [7]. Also, it is worth realizing that the crack path followed the boundaries of the pearlitic colony that underwent the episode of decohesion as indicated by dashed yellow circles in **Figures 5 (h)** and **(i)**. In addition to this, another event of decohesion was identified during the UC's rupture in **Figure 5 (i)**, which resulted in an almost detached colony (denoted by a blue brace) where its remaining decohesion region is pointed out by a blue arrow. In this situation, the crack also seemed to cross some GBs-α (pointed out by red arrows) and other boundaries of pearlitic colonies as indicated by the dashed yellow arrows and underlined by the dashed orange line in **Figures 5 (h)** and **(i)**.

Based on the evidence provided during the UC's in-situ TS experiment, it is reasonable to consider that in the pearlitic microstructure of UC, the rotation mechanism caused by the shear progress resulted in a significantly stretched pearlitic microstructure near the maximum principal stress direction. Conversely, the UC's big pearlitic colonies seemed to be compressed and smashed against each other in a direction close to the minimum principal stress component. In this context, it is plausive to assume that the colony boundaries were highly strained due to their discontinuous lamellar arrangement. In contrast, the regions inside the colonies underwent a more homogenous deformation because there are more cementite lamellae uniformly distributed. Therefore, the colonies tend to slide against each other through the deformation of their colony's boundaries under shear which can result in colony decohesion. However, dissimilar morphology of cementite within the colony can develop strain concentration. As a consequence, this instability is able to cause breakages of the neighbor cementite lamellae. In view of this, the phenomenon of decohesion between colonies can lead to crack initiation or an easier path of crack propagation such as at the GBs-α regions. Moreover, the big pearlitic blocks of UC may allow a fast crack propagation conducting a quick detachment during its failure.

Now regarding the behavior of the DR specimen under TS deformation, no broken cementite was found in 1RD (**Figures 6 (a)**, **8 (a)**, and **8 (b)**). Then, concerning the RD's necking stage, a small rotation can be realized through the tracking of the GBs-α movement in 2DR (**Figures 6 (b)**, **8 (d)**, and **8 (e)**). At the same time, some cementite lamellae were bent as pointed out in **Figure 8 (e)**. In this context, the shear strain (-0.35) started to be concentrated mainly in some GBs-α regions as indicated by white arrows in **Figure 8 (f)**. After that, the microstructural rotation gradually increased in addition to a no longer smooth specimen surface due to plastic deformation in 3DR (**Figures 6 (d)**, **8 (g)**, and **8 (h)**) and 4DR (**Figures 6 (e)**, **8 (j)**, and **8 (k)**) images. Also, many buckled cementite lamellae were found in RD condition (see **Figures 8 (h)**, and **(k)**) instead of breaking as in the UC sample. This behavior supports that thin cementite lamellae present greater plastic deformability than coarse ones [32]. Under this circumstance, the RD's pearlitic colonies seemed to be very rigid and no severe readjustment into the diagonal direction

was realized during the TS experiment such as it was in UC. This fact is confirmed by the DIC analysis in **Figure 6 (f)** which revealed distortion angles in 4DR over 50° about the shear direction. Moreover, the highest strained regions found in 3DR and 4DR were still in the GBs-α in addition to one pearlitic colony. This sharply strained pearlitic colony has lamellae parallel to the shear components and seems to undergo interlamellar decohesion. Furthermore, in contrast to CU, the fracture detachment happened slowly and gradually in the DR specimen, as shown in **Figures 6 (g)** and **(h)**, which may indicate an influence of its smaller pearlitic block [7]. Finally, the orientation of the rupture in DR was similar to the UC which demonstrates again the effect of the principal stresses imposed by the shear condition.

Finally, even though all aforementioned finds about the DR specimen, it was not clearly detected sites where cracks can start to nucleate or signs of the main paths for cracks propagate throughout the DR's microstructure, probably, due to its refined condition. Thus, the DR specimen was additionally and subsequently investigated by the interrupted TS experiment technique.

3.3 Interrupted shear-tensile (TS) experiment of DR specimen

Concerning the aforementioned issue related to the DR's refined microstructure during the SEM in-situ observation, this section specifically focuses on designing a possible mechanism for DR's mode failure through EBSD, SE, and BSE interrupted analyses. These investigations were performed before (start condition) and after (at the failure instant) the TS experiment preserving the same area. The elongation-load curve obtained from the interrupted TS experiment is displayed in **Figure 9 (a)** evidencing both evaluated circumstances: Before and After. From the viewpoint of accuracy, it is relevant to highlight that DR provided a similar elongation-load curve behavior in both TS proceedings implemented in this work (see **Figures 4** and **9 (a)**).

In view of this, **Figure 9 (b)** and **(c)** show, respectively, the IPF map and its BSE image of the DR specimen before the TS test. This setup provides information about the crystallographic orientation of the ferritic matrix and the geometric lamellar orientation of the pearlites in the investigated region. Also, GBs-α were detected in the BSE image as indicated by the white arrows in **Figure 9 (c)**. Likewise, **Figure 9 (d)** exhibits the IPF map of the DR condition after the TS experiment preserving the initial area displayed in **Figure 9 (b)**. In this case, there are many dark (not indexed) regions in the IPF map after TS deformation that seem to be potential zones of initial cracks. However, to confirm the presence of these defects, BSE and SE images available, respectively, in **Figures 9 (e)** and **(f)** were also acquired from the same IPF map area at the failure instant. In this regard, the initial cracks in the BSE image were not validated because they had a smooth superficial relief and the potential cracks looked like scratches as seen in **Figure 9 (e)**. Conversely, the SE image, in **Figure 9 (f)**, supplied suitable relief information that could confirm the cracked region surrounded by a white dashed irregular circle. This zone rich in cracks involves mainly a pearlitic colony comprised of an initially ND//<111> oriented ferritic matrix (blue orientation) and lamellae of cementite geometrically orientated nearly parallel to the shear stress components. Therefore, those cracks, following the same spatial orientation of the pearlitic lamellae, seem to be originated through the phenomenon of decohesion at the ferrite/cementite interface (interlamellar) since the yielding in pearlite colonies occurs predominately via plastic deformation in the ferritic lamellae [33]. Moreover, it is worth noting the development of three violet sections (new orientation) in the ferrite lamellae of the cracked and detached region in **Figure 9 (d)**. These linear segments, aligned around 46.7°, 51.6°, and 57.3° about the tensile direction, are evidence of favorable local lattice rotation or local

deformation (shear band) in the initially {111} orientated ferritic matrix during the shear progress.

Additionally, work hardening in pearlitic steel is attributed to phase stresses caused by the misfit strains (dislocation pile-ups) at the ferrite/cementite interface [34]. Also, plastic deformation can modify the lattice structure of cementite plates strengthening them against breakage[4]. Again, it is well known that pearlitic colonies with their lamellae aligned parallelly to the tensile direction hold dislocation slippage[2,5]. Moreover, according to Kestens and Pirgazi, (2016)[35] the <111> crystallographic orientation in BCC metals provides favorable dislocation motion due to its closest-packed direction. Therefore, it is reasonable to suggest that the ND//<111> ferritic lamellae in the pearlitic colony enclosed by the dashed nonuniform circle in **Figures 9 (d)**, **(e)**, and **(f)** had preferential activation of their primary slip plans during the shear procedure. As a result, it will promote easier plastic deformation (dislocation motion) and produce new dislocations in those ferritic lamellae. However, the hard geometrical orientation of the lamellar cementite acts as a barrier to that ferritic dislocation movement which may increase the misfit strain initiated by the work hardening mechanism. Moreover, although the cementite plates with higher yield strength do not break, they cannot accompany the same dimensional distortion experienced by the ferritic lamellae. As a consequence, local stress tends to increase at the ferrite/cementite interface leading to the event of decohesion that will work as a crack nucleation source during shear deformation.

Furthermore, considering microtexture modification during the DR's interrupted TS experiment, **Figures 9 (g)** and **(h)** present the ODFs measured from the DR's IPF maps in the conditions Before and After, respectively. Based on this, the condition Before shows microtexture components around the γ (ND//<111>) fiber which was likely produced during the prior ≈65% cold-rolling process [23]. However, this initial microtexture exhibited asymmetry of components and their intensities with a maximum of 6.4 mrd around the {111}<123> and {111}<112> orientations. This design of orientation distribution can be an influence of the repeated tension and compression stresses introduced in the surface of DR's specimen by the previous four consecutive bending procedures [34,36]. Moreover, the γ fiber was considered as a reference for evaluating the crystallographic rotation in the DR specimen between the Before and After TS conditions. This fiber is indicated by a continuous line in both ODFs, and their intensities were plotted in **Figure (i)**. In this context, it is possible to observe that TS's deformation resulted in a reduction of the initial microtexture intensity with a new maximum of 4.2 mrd. This agreed with the study of Guo et al. (2015)[1]. These authors demonstrated that the development of shear deformation in pearlitic steel tended to shift the microtexture into a random state (weaker microtexture). Additionally, **Figure 9 (h)** reveals a smooth improvement in the symmetry of the component distribution that may be a consequence of lattice rotations during the TS procedure. In this way, a small crystallographic rotation (with a maximum of 9.1°) was identified between the two characterized conditions along the γ fiber. It is consistent with the rigid microstructural behavior of DR conferred during its in-situ investigation. In addition to this, cracks were not detected around the GBs-α.

Regarding the prior outcomes of the DR's in-situ inspection and the support of the present topic with the interrupted TS test evaluation, it can be implied that the development of shear in the DR's microstructure occurs mainly through the deformation of GBs-α, while most of the pearlite colonies are kept rigid up to the decohesion of some colonies aligned parallel to the shear components, specifically, those who has easily activation of ferritic slip plans which are able to provide a higher gradient of distortion between the hardly deformable cementite plates and

softer ferrite lamellae. Likewise, other lamellar pearlitic colonies aligned almost parallel to the shear components were also found with similar crack behavior as shown in **Figure 10**.

3.4 Fracture surfaces

The purpose of the current topic is to explore the fracture surface of UC (**Figure 11**) and DR (**Figure 12**) specimens after their rupture during the in-situ TS experiments. The fractography indicates a ductile shear failure mode in both investigated conditions. In this way, two categories of shear fractures were identified: with dimples (Region I) and with flat surfaces (Region II) as indicated in **Figures 11 (a)** and **12 (a)**. In detail, UC exhibited a shear fracture predominantly with a flat surface that corresponds to 97.7% of the fractured area. The other remaining 2.3% of the UC's area is abundant in dimples (Region I) and located close to the center of its fractured surface as shown in **Figures 11 (a)**, **(b),** and **(c)**. In contrast, DR presented mostly of its shear fractured area containing dimples (84.4%), while **Figures 12 (a)** and **(b)** display the laterals of DR's fracture surface that are comprised of flat surfaces that represent 15.6% of DR's total fractured area.

In all Region I (in **Figures 11 (c)**, **12 (c)**, **12 (d)**, **12 (e)**, **12 (f)**, and **12 (g)**), there are many small, shallow, and ellipsoid-shaped dimples that are elongated about the shear direction. These morphological aspects can be attributed to the large plastic deformation caused by the shear process that relaxes the stress concentration around the voids initially nucleated under the maximum normal tensile stress. As a result, the voids are not able to grow and coalesce into the normal stress direction. However, local shear bands among void ligaments will be activated and propagated in the direction of the maximum shear stress. This mechanism will promote the growth of the voids into a parabolic shape and then, they will be shear-linked up resulting in the final fracture surface [31]. On the other hand, all Region II (in **Figures 11 (d)**, **11 (e)**, **11 (f)**, **11 (g)**, and **12 (b)**) are composed of smooth zones that apparently are deficient in dimples. In this case, it is pointed out by the literature [37] that the shear plastic deformation is too large that voids will not be produced by the maximum normal tensile stress, unlikely a significant plastic slip will be the main mechanism providing many shear bands. As a consequence, the intensive propagation of these local strained bands will develop an integrated shear fracture surface poor in dimples.

Furthermore, it can be seen in **Figures 11 (e)** and **(g)** that the smooth fractured surface on UC is also constituted by dimples. These dimples are considerably more oriented to the shear direction than those on the DR fracture. It suggests dimples formation by shear stress. In addition to this, UC underwent a great macroscopic plastic deformation before failure, as previously depicted in **Figure 5 (g)**. These facts suggest that UC may have established a significant alignment of its shear bands into the maximum shear stress direction. Additionally, an increase in grain size contributes to microstructural instability during the plastic deformation, which makes the grains prone to develop shear bands [15,30,38]. In this regard, it is known from the literature [15] that microstructural coarsening tends to change the fracture mechanism from shear fracture with voids to shear fracture with a flat surface. Therefore, the bigger pearlitic blocks of UC may have led to its shear rupture with a flat surface by boosting plastic deformation closely to the shear stress direction, which may result in a weak influence of the normal stress. Additionally, the UC failure surface presents some secondary cracks and large flat detached regions with high topographic relief, as indicated in Figures **11 (a)**, **11 (b)**, and **11 (d)**. Concerning the very soft microstructure of UC, these features can be a consequence of microstructural heterogeneity and hard second-phase particles such as inclusions [15,39]. In this regard, those enormous flat detached structures seemed to be slip plans of pearlitic blocks that underwent transgranular fracture achieving sizes around 123 µm. In this context, **Figure 13** confirms that

the pearlitic blocks in UC have a comparable dimensional magnitude (around 168 µm) to the flat areas with high topography in the UC's surface fracture. This evidence may suggest the presence of large slip plans due to the UC's coarse pearlitic blocks.

Moreover, many researchers[40-42] reveal that shear fracture with a flat surface presents lesser shear strength and occurs faster in contrast to shear fracture with dimples. This phenomenon agreed with the aforementioned ruptures behavior during the in-situ TS experiments in which UC abruptly failed and DR does not. From this perspective, the smooth fracture surface of DR is mainly concentrated on the edge of the rupture plane. It may indicate that the DR's fracture started slowly in the areas rich in dimples and ended up fast in the zone comprised of a flat surface such as shear lips [43]. Finally, the rupture in UC should also occur following the same steps just described for DR, however, the fractured region in UC that is rich in dimples is too small that its effect on the entire failure is irrelevant, resulting in a dominance of the fast failure behavior.

4. Conclusion

In-situ tensile-shear (TS) tests in scanning electron microscopy (SEM) and digital image correlation (DIC) technique were performed for two types of pearlitic steel microstructure: undeformed-coarse (UC) and deformed-refined (DR). In this context, the following conclusions can be drawn:

- The geometry of the TS specimen adopted in the in-situ SEM experiments proved to be suitable for providing easier access to the pearlitic microstructure surface under shear deformation.
- The DR pearlitic microstructure exhibited higher shear strength than the UC pearlitic condition during shear deformation. However, DR elongated less than UC.
- The DIC identified strain heterogeneity in both pearlitic steel conditions under shear deformation. In the softer microstructure of the UC condition, the strain was concentrated mainly at the pearlitic colony boundary. Regarding the rigid microstructure of the DR specimen, the strain was located in grain boundary ferrite and in particular pearlites with lamellae aligned parallel to the tensile axis.
- The phenomenon of decohesion was the main mechanism observed to be a potential source of crack initiation in both studied pearlitic steel microstructures. Specifically, decohesion happened at the colony boundary in the UC microstructure and at the ferrite/cementite interface (interlamellar) in the DR pearlitic condition.
- Cementite showed to break easily in the UC condition as the tensile-shear test progressed and it tended to buckle in the DR pearlitic state.
- The UC and DR pearlitic microstructures led to different shear failure modes. The UC pearlitic steel underwent an instantaneous rupture and its sheared fracture surface presented a flat aspect. In contrast, the failure of the DR specimen occurred slowly and its fractured surface was abundant in dimples.

Acknowledgments

The authors acknowledge with gratitude the team of the Materials Characterization Laboratory

(LACAM), Analytical Central from Federal University of Ceará (UFC), the Ohio State University (OSU), the Manufacturing and Materials Joining Innovation Center (MA2JIC), and the Center for Electron Microscopy and Analysis (CEMAS), the Research and Support Foundation of Maranhão (FAPEMA), Brazilian Federal Agency for Support and Evaluation of Graduate Education (CAPES) and Brazilian National Council for Scientific and Technological Development (CNPq).

References

[1] Guo N, Song B, Wang B-S, Liu Q. Influence of torsion deformation on textures of cold drawing pearlitic steel wires. Acta Metall Sin 2015;28:707-14. https://doi.org/10.1007/s40195-015-0251-7

[2] Durgaprasad A, Giri S, Lenka S, Sarkar SK, Biswas A, Kundun S, et al. Delamination of pearlitic steel wires: the defining role of prior-drawing microstructure. Metall Mater Trans A 2018;49:2037-47. https://doi.org/10.1007/s11661-018-4564-9

[3] Hu X, Wang L, Fang F, Ma Z, Xie Z-h, Jiang J. Origin and mechanism of torsion fracture in cold-drawn pearlitic steel wires. J Mater Sci 2013;48:5528-35. https://doi.org/10.1007/s10853-013-7347-0

[4] Zhou L, Fang F, Wang L, Hu X, Xie Z, Jiang J. Torsion performance of pearlitic steel wires: effects of morphology and crystallinity of cementite. Mater Sci Eng A 2019;743:425-35. https://doi.org/10.1016/j.msea.2018.11.113

[5] Teshima T, Kosaka M, Ushioda K, Koga N, Nakada N. Local cementite cracking induced by heterogeneous plastic deformation in lamellar pearlite. Mater Sci Eng A 2017;679:223-9. https://doi.org/10.1016/j.msea.2016.10.018

[6] Koga N, Nakada N, Tsuchiyama T, Takaki S, Ojima M, Adachi Y. Distribution of elastic strain in a pearlitic structure. Scr Mater 2012;67(4):400-3. https://doi.org/10.1016/j.scriptamat.2012.05.034

[7] Zhou S, Zuo Y, Li Z, Wang X, Yong Q. Microstructural analysis on cleavage fracture in pearlitic steels. Mater Charact 2016;119:110-3. https://doi.org/10.1016/j.matchar.2016.07.023

[8] Lewandowski JJ, Thompson AW. Effects of the prior austenite grain size on the ductility of fully pearlitic eutectoid steel. Metall Mater Trans A 1986;17:461–72. https://doi.org/10.1007/BF02643953

[9] Mishra K, Khiratkar VN, Singh A. Change of deformation mechanism through nano-structuring of pearlite: An in-situ study. Mater Charact 2020;167:110487. https://doi.org/10.1016/j.matchar.2020.110487

[10] Hyzak JM, Bernstein IM. The role of microstructure on the strength and toughness of fully pearlitic steels. Metall Trans A 1976;7:1217–24. https://doi.org/10.1007/BF02656606

[11] Durgaprasad A, Giri S, Lenka S, Kundu S, Chandra S, Mishra S, et al. Microstructural engineering in eutectoid steel: a technological possibility?. Metall Mater Trans A 2018;49:1520-35. https://doi.org/10.1007/s11661-018-4501-y

[12] Guo N, Song B, Luan B, Chen Z, Liu Q. Deformation bands in fully pearlitic steel during wire drawing. Sci China Technol Sci 2014; 57:796-803. https://doi.org/10.1007/s11431-013-5434-8

[13] Tagashira S, Sakai K, Furuhara T, Maki T. Deformation microstructure and tensile strength of cold rolled pearlitic steel sheets. Isij International 2000;40(11):1149-56. https://doi.org/10.2355/isijinternational.40.1149

[14] Takahashi T, Nagumo M, Asano Y. Microstructures Dominating the Ductility of Eutectoid Pearlitic Steels. J Jpn Inst Metals 1978;42(7):708–15. https://doi.org/10.2320/jinstmet1952.42.7_708

[15] Li Z, Yang X, Tang A. A Fracture Criterion for Prediction of Fracture Initiation of Metal Materials at Various Stress States for Nuclear Waste Storage. Sci Technol Nucl 2019;2019:3591925. https://doi.org/10.1155/2019/3591925

[16] Nine HD. Slip planes and asymmetric slip in fatigue of iron single crystals. Phil Mag 1972;26(6): 1409-18. https://doi.org/10.1080/14786437208220351

[17] Inoue A, Ogura T, Masumoto T. Deformation and fracture behaviours of cementite. Trans Jpn Inst Met 1976;17(10):663-72. https://doi.org/10.2320/matertrans1960.17.663

[18] Vermeij T, Hoefnagels JPN. Plasticity, locatization, and damage in ferritic-pearlitic steel studied by nanoscale digital image correlation. Scr Mater 2022;208:114327. https://doi.org/10.1016/j.scriptamat.2021.114327

[19] Isavand S, Assempour A. Strain localization and deformation behavior in ferrite-pearlite steel unraveled by high-resolution in-situ testing integrated with crystal plasticity simulations. Int J Mech Sci 2021;200:106441. https://doi.org/10.1016/j.ijmecsci.2021.106441

[20] Yajima Y, Koga N, Watanabe C. Influential factors on the deformability of colonies in pearlitic steel. Mater Charact 2021;177:111197. https://doi.org/10.1016/j.matchar.2021.111197

[21] Cordier-Robert C, Forfert B, Bolle B, Fundenberger J-J. Tidu A. Influence of torsion deformation on microstructure of cold-drawn pearlitic steel wire. J Mater Sci 2008; 43:1241-8. https://doi.org/10.1007/s10853-007-2272-8

[22] Fang F, Zhou L, Hu X, Zhou X, Tu Y, Xie Z, et al. Microstructure and mechanical properties of cold-drawn pearlitic wires affect by inherited texture. Mater Des 2015;79:60-7. http://dx.doi.org/10.1016/j.matdes.2015.04.036

[23] Leão PBP, Zhang S, Neto JRB, Freire SA, Loureiro RCP, Ramirez AJ, et al. Microstructure, microtexture, and crack susceptibility in pearlitic steel during lab-simulated processes aiming tensile armor application in flexible pipelines. J Mater Process Technol 2023;316:117950. https://doi.org/10.1016/j.jmatprotec.2023.117950

[24] Fernando US, Davidson M, Yan K, Roy MJ, Pirling T, Withers PJ, et al. Evolution of residual stress in tensile armour wires of flexible pipes during pipe manufacture. In: Proceeding of the ASME 2017 36th International Conference on Ocean, Offshore and Arctic Engineering, 2017, Trondheim, Norway.

[25] Aranda MM, Kim B, Rementeria R, Capdevila C, García de Andrés C. Effect of Prior Austenite Grain Size on Pearlite Transformation in a Hypoeuctectoid Fe-C-Mn Steel. Metall Mater Trans A 2014;45: 1778–86. https://doi.org/10.1007/s11661-013-1996-0

[26] Miyamoto G, Karube Y, Furuhara T. Formation of grain boundary ferrite in eutectoid and hypereutectoid pearlitic steels. Acta Mater 2016;1031;370–81. https://doi.org/10.1016/j.actamat.2015.10.032

[27] Zhang S, Romo S, Giorjão RA, Leão PBP, Ramirez AJ. EBSD analysis of strain distribution and evolution in ferritic-Pearlitic steel under cyclic deformation at intermediate temperature. Mater Charact 2022; 193:112293. https://doi.org/10.1016/j.matchar.2022.112293

[28] Wright S, Nowell M, Field D. A review of strain analysis using electron backscatter diffraction. Microsc Microanal 2011;17(3):316–29. https://doi.org/10.1017/S1431927611000055

[29] Li YJ, Choi P, Borchers C, Westerkamp S, Goto S, Raabe D, Kirchheim R. Atomic-scale mechanisms of deformation-induced cementite decomposition in pearlite. Acta Mater 2011;59(10):3965-77. https://doi.org/10.1016/j.actamat.2011.03.022

[30] Behera S, Barik RK, Sk MB, Mitra R, Chakrabarti D. Recipe for improving the impact toughness of high-strength pearlitic steel by controlling the cleavage cracking mechanisms. Mater Sci Eng A 2019;764(9):138256. https://doi.org/10.1016/j.msea.2019.138256

[31] Dieter GE. Mechanical Metallurgy. 3rd Edition, McGraw-Hill book company, United States, 1986

[32] Umemoto M, Todaka Y, Tsuchiya K. Mechanical properties of cementite and fabrication of artificial pearlite. Mater Sci Forum 2003;426-432:859-64. https://doi.org/10.4028/www.scientific.net/MSF.426-432.859

[33] Tomota Y, Watanabe O, Kanie A, Moriai A, Minakawa N, Moriai Y. Effect of carbon concentration on tensile behavior of pearlitic steels. Mater Sci Technol 2003;19(12):1715–20. https://doi.org/10.1179/026708303225008310

[34] Wang Y, Tomota Y, Harjo S, Gong W, Ohmura T. In-situ neutron diffraction during tension-compression cyclic deformation of a pearlite steel. Mater Sci Eng A 2016;676:522-30. https://doi.org/10.1016/j.msea.2016.08.122

[35] Kestens LAI, Pirgazi H. Texture formation in metal alloys with cubic crystal structures. Mater Sci Technol 2016;32(13):1303–15. https://doi.org/10.1080/02670836.2016.1231746

[36] Mehrabi H, Yang R, Wang B. Effects of Tension–Compression Asymmetry on Bending of Steels. Appl Sci 2020;10(9): 3339. https://doi.org/10.3390/app10093339

[37] Li Z, Shi J, Tang A. Investigation on fracture mechanisms of metals under various stress states. Acta Mech 2014;225:1867–81. https://doi.org/10.1007/s00707-013-1024-x

[38] Jazaeri H, Humphreys FJ. The effect of initial grain size on the microstructures developed during cold rolling of a single-phase aluminium alloy. Msf 2004;467–4701:63-68. https://doi.org/10.4028/www.scientific.net/MSF.467-470.63

[39] Barsoum I, Faleskog J. Rupture mechanisms in combined tension and shear—Experiments. Int J Solids Struct 2007;44(6):1768–86. https://doi.org/10.1016/j.ijsolstr.2006.09.031

[40] Chen C-H, Sun Y-K, Lai Y-C, Chang S-Y, Chuang T-H. Effect of Post-Weld Heat Treatment on the Solid-State Diffusion Bonding of 6061 Aluminum Alloy. Appl Sci 2021;11(20):9660. https://doi.org/10.3390/app11209660

[41] Karthikeyan KMB, Yuvaraj C, Balasubramanian T. Tensile test fractography of subzero treated EN24 alloy steel. Mater Today 2021;46:3205-11. https://doi.org/10.1016/j.matpr.2020.11.192

[42] Han B, Sun F, Li T, Liu Y. Shear strength, fracture mechanism and plastic performance of Cu/Sn5Sb–xCuNiAg/Cu solder joints during thermal aging. J Mater Sci: Mater Electron 2019;30:18342-9. https://doi.org/10.1007/s10854-019-02188-x

[43] Kiran R, Asce SM, Khandelwal K. Experimental Studies and Models for Ductile Fracture in ASTM A992 Steels at High Triaxiality. J Struct Eng 2014;140(2). https://doi.org/10.1061/(ASCE)ST.1943-541X.0000828

Table 1. Chemical composition of the as-received pearlitic steel (wt%).

C	Mn	Si	S	P	Cr	Ni	V	Al	Ti	Fe
0.736	0.648	0.227	0.006	0.011	0.179	0.023	0.004	0.023	0.003	Bal.

Table 2. Summary of the initial microstructure characteristics of the undeformed-coarse (UC) and deformed-refined (DR) pearlitic steel conditions.

Sample's name	Average of interlamellar spacing (nm)	Average of Colony size (μm)	Volume fraction of GB-α (%)	Number fraction concentration of the morphological angle (°)	Overall average of KAM (°)	Density of LABs (μm/μm²)	Density of MABs (μm/μm²)	Density of HABs (μm/μm
UC	402.6 ± 64.4	16.0 ± 3.9	5.6	20-30 / 60-70	0.6 ± 0.4	0.03	0.02	0.10
DR	173.2 ± 37.6	9.9 ± 1.6	4.3	0-10	2.1 ± 1.1	2.92	1.51	0.93

Table 3. Structural properties and microhardness average of the undeformed-coarse (UC) and deformed-refined (DR) conditions.

Sample name	Elastic stiffness (N/µm)	Ultimate load (N)	Ultimate elongation (µm)	Absorbed energy (KJ)	Microhardness average ($HV_{0.2}$)
UC	2.8	312.5	325.6	77.7	223.1 ± 11.2
DR	7.0	646.8	209.8	102.6	409.4 ± 7.9

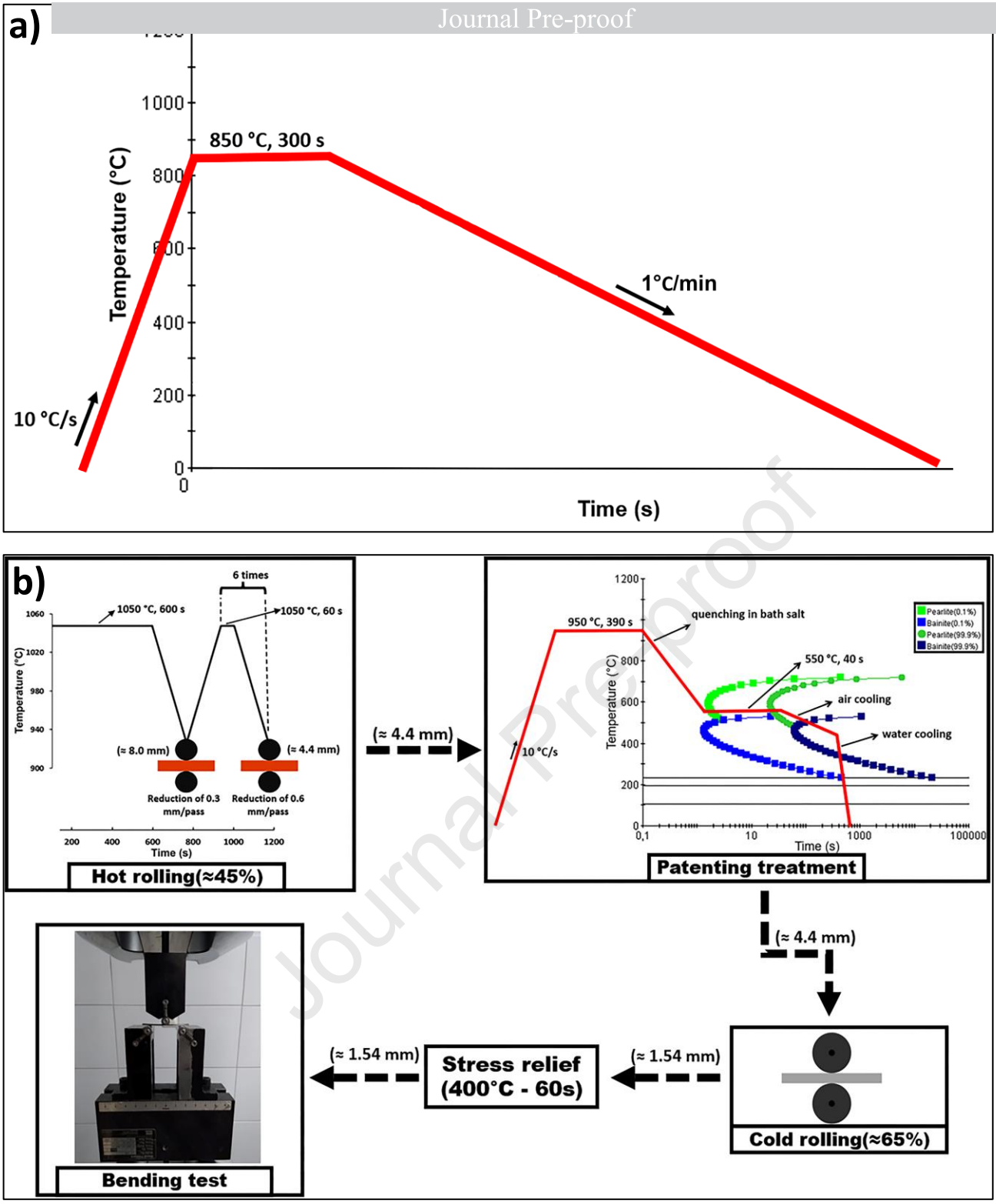

Figure 1. Schematic proceedings employed in this work to produce the start investigated pearlitic steel conditions. **(a)** Diagram with representative details of the thermal treatment with slow cooling performed in the undeformed-coarse (UC) specimen **(b)** Illustrative flowchart of the laboratory processing route undergone by the deformed-refined (DR) specimen. The numbers in millimeters (mm) contained in Figure 1 (b) represent the samples' thickness.

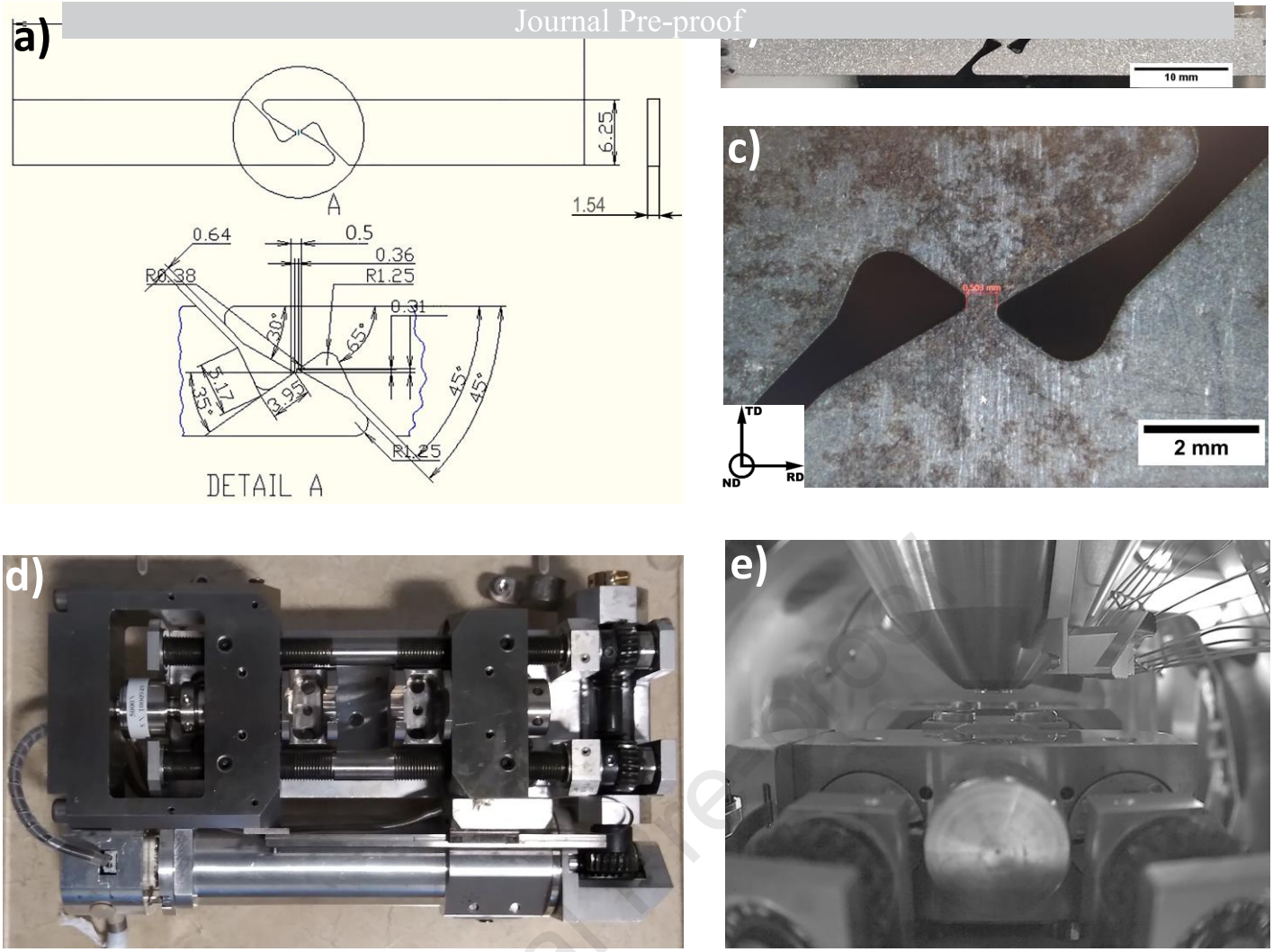

Figure 2. Details of the In-situ shear experiment implemented in this work. **(a)** Sketch of the tensile-shear specimen geometry with its dimensions in millimeters. **(b)** Machined tensile-shear specimen. **(c)** Central region of the tensile-shear specimen. **(d)** Kammrath-Weiss tensile stage. **(e)** The tensile stage set up in the scanning electron microscope chamber.

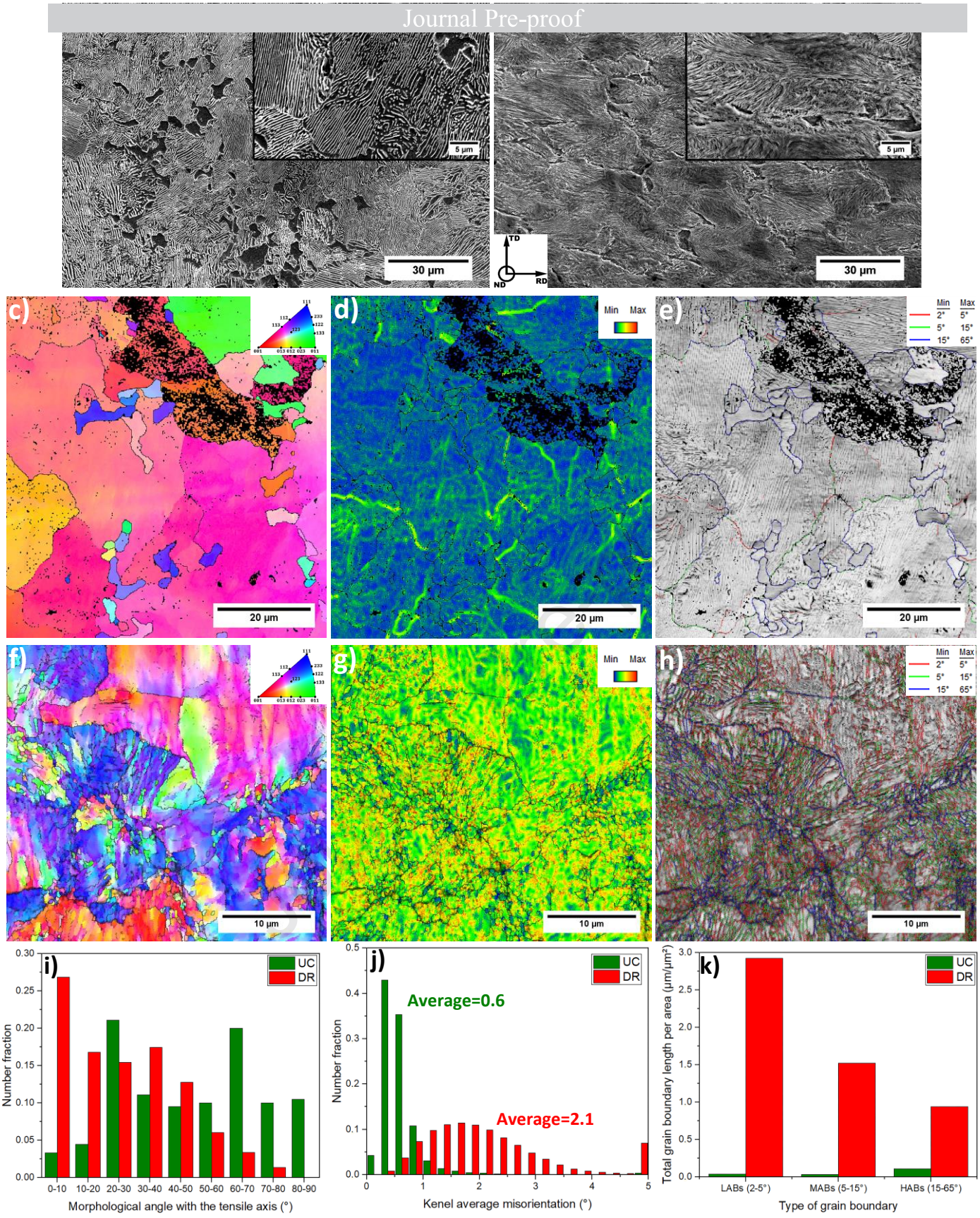

Figure 3. Initial metallurgical characteristics of the undeformed-coarse (UC) and deformed-refined (DR) pearlitic steel conditions. Start scanning electron microscope (SEM) microstructures of the **(a)** UC and **(b)** DR samples. Color-coded inverse pole figure (IPF) map, kernel average misorientation (KAM) map, and grain boundary distribution map, respectively, for the **(c)(d)(e)** UC and **(f)(g)(h)** DR conditions. **(i)** Distribution of the pearlitic morphological angles about the tensile axis, **(j)** distribution of KAM values, and **(k)** distribution of grain boundary type per area for UC and DR.

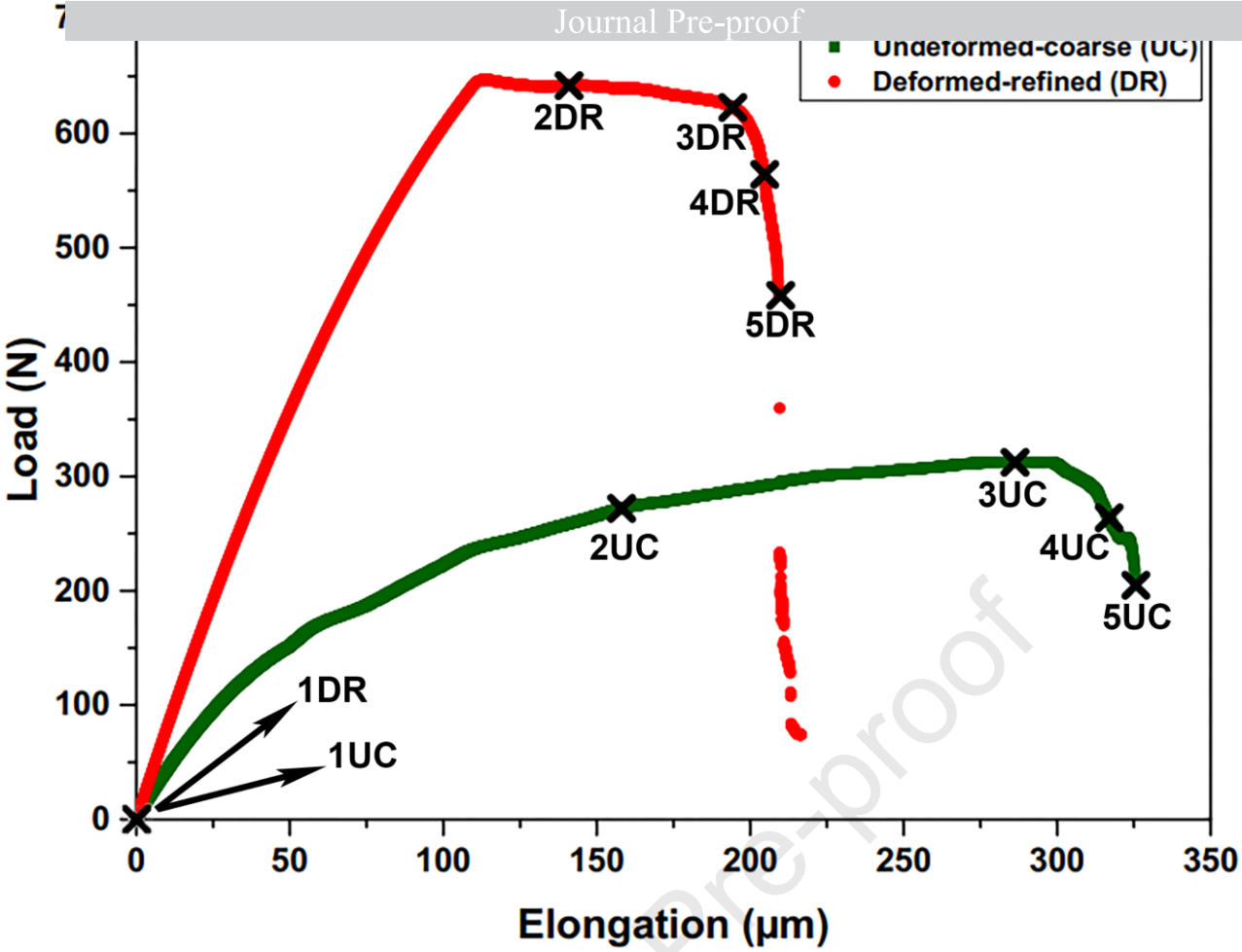

Figure 4. Elongation-load curves obtained during the in-situ tensile-shear test for undeformed-coarse (UC) and deformed-refined (DR) pearlitic steel conditions. The points marked with x represent the stages where the captured scanning electron microscope (SEM) images were selected for demonstrating the progress of the tensile-shear experiment.

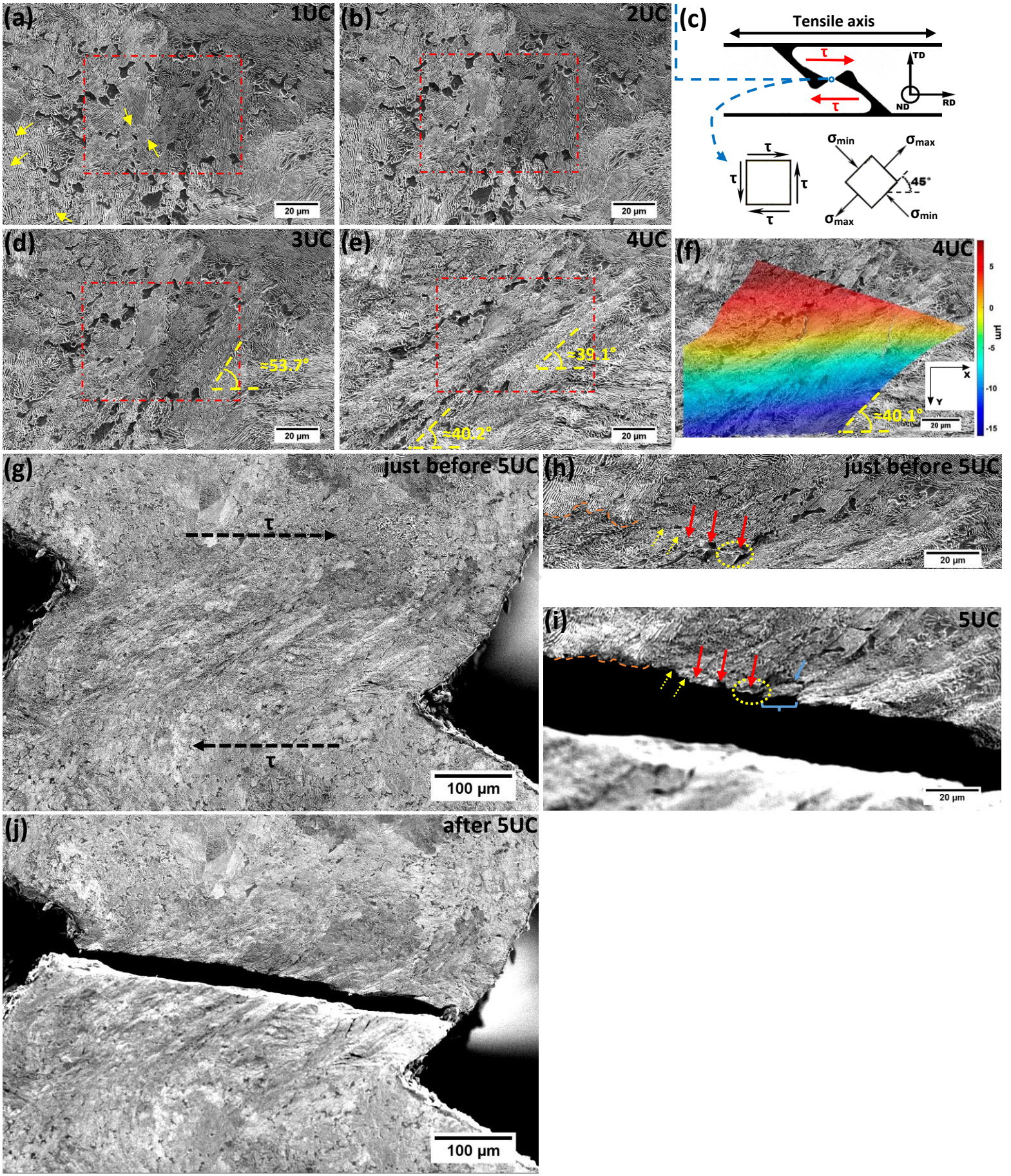

Figure 5. Macro scanning electron microscope (SEM) images of the undeformed-coarse (UC) specimen's deformation during the in-situ tensile-shear test following, as a reference, the x-marks in its elongation-load curve (see Figure 4): **(a)** 1UC, **(b)** 2UC, **(d)** 3UC, **(e)** 4UC, **(g)** just before 5UC in a lower magnification, **(h)** just before 5UC in the regular magnification, **(i)** 5UC, **(j)** after 5UC in a lower magnification. **(c)** Illustrative diagram reference of the stress components and geometrical analysis position during the in-situ tensile-shear test. **(f)** Eulerian *u*-displacement map obtained via digital image correlation (DIC) from the 1UC up to the 4UC stage. The red dashed rectangles represent the region where the images in high magnification of **Figure 7** were taken.

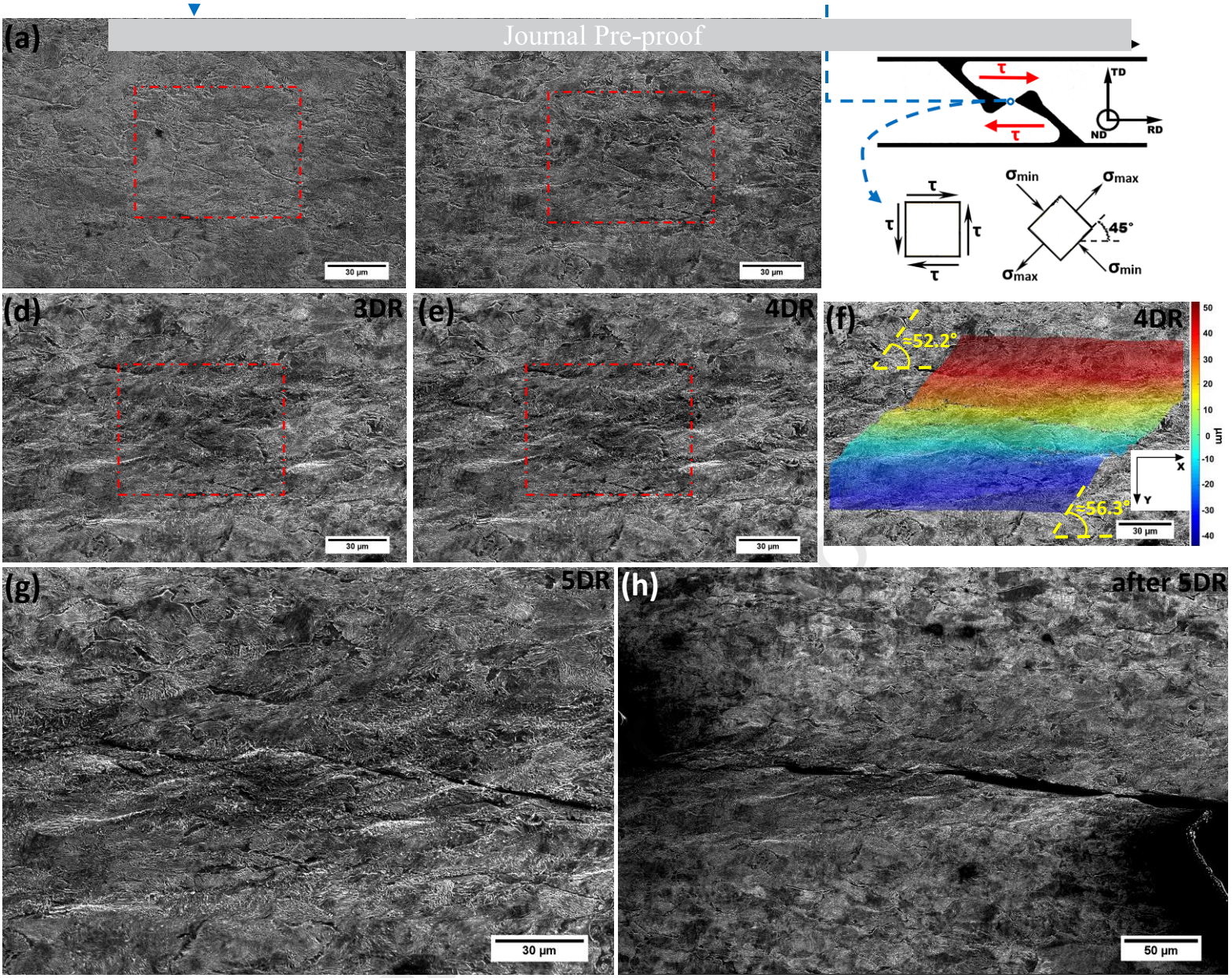

Figure 6. Macro scanning electron microscope (SEM) images of the deformed-refined (DR) specimen's deformation during the in-situ tensile-shear test following, as a reference, the x-marks in its elongation-load curve (see Figure 4): **(a)** 1DR, **(b)** 2DR, **(d)** 3DR, **(e)** 4DR, **(g)** 5DR, and **(h)** after 5DR. **(c)** Illustrative diagram reference of the stress components and geometrical analysis position during the in-situ tensile-shear test. **(f)** Eulerian *u*-displacement map obtained via digital image correlation (DIC) from the 1DR up to the 4DR stage. The red dashed rectangles represent the region where the images in high magnification of **Figure 8** were taken.

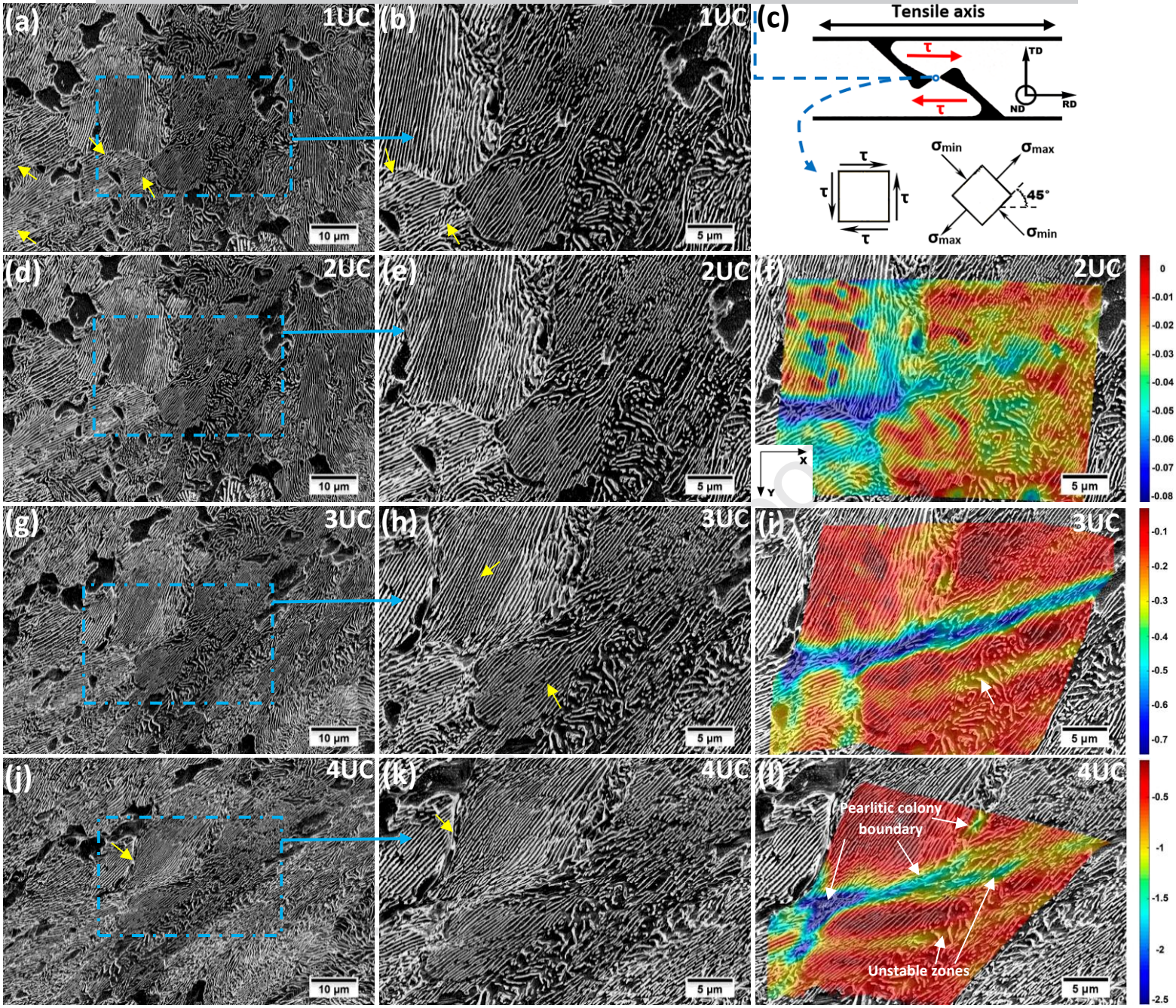

Figure 7. High magnification scanning electron microscope (SEM) images of the undeformed-coarse (UC) specimen's deformation during the in-situ tensile-shear test following, as a reference, the x-marks in its elongation-load curve (see Figure 4): **(a) (b)** 1UC, **(d) (e)** 2UC, **(g) (h)** 3UC, and **(j) (k)** 4UC. **(c)** Illustrative diagram reference of the stress components and geometrical analysis position during the in-situ tensile-shear test. **(f) (i) (l)** Eulerian shear strain maps, e_{xy}, obtained via digital image correlation (DIC), in the respective stages 2CU, 3CU, and 4CU of the UC's elongation-load curve in **Figure 4**.

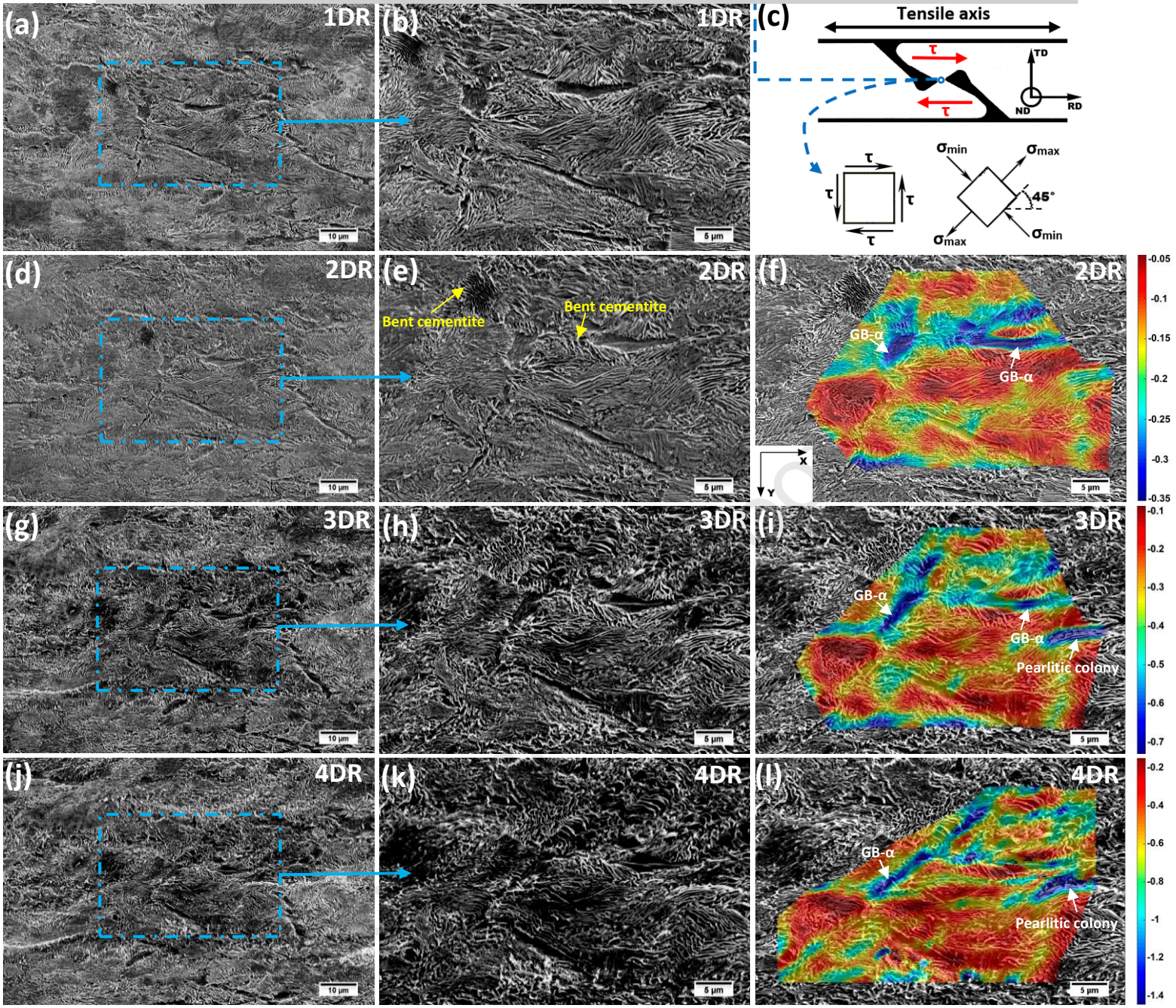

Figure 8. High magnification scanning electron microscope (SEM) images of the deformed-refined (DR) specimen's deformation during the in-situ tensile-shear test following, as a reference, the x-marks in its elongation-load curve (see Figure 4): **(a) (b)** 1DR, **(d) (e)** 2DR, **(g) (h)** 3DR, and **(j) (k)** 4DR. **(c)** Illustrative diagram reference of the stress components and geometrical analysis position during the in-situ tensile-shear test. **(f) (i) (l)** Eulerian shear strain maps, e_{xy}, obtained via digital image correlation (DIC), in the respective stages 2DR, 3DR, and 4DR of the DR's elongation-load curve in **Figure 4**.

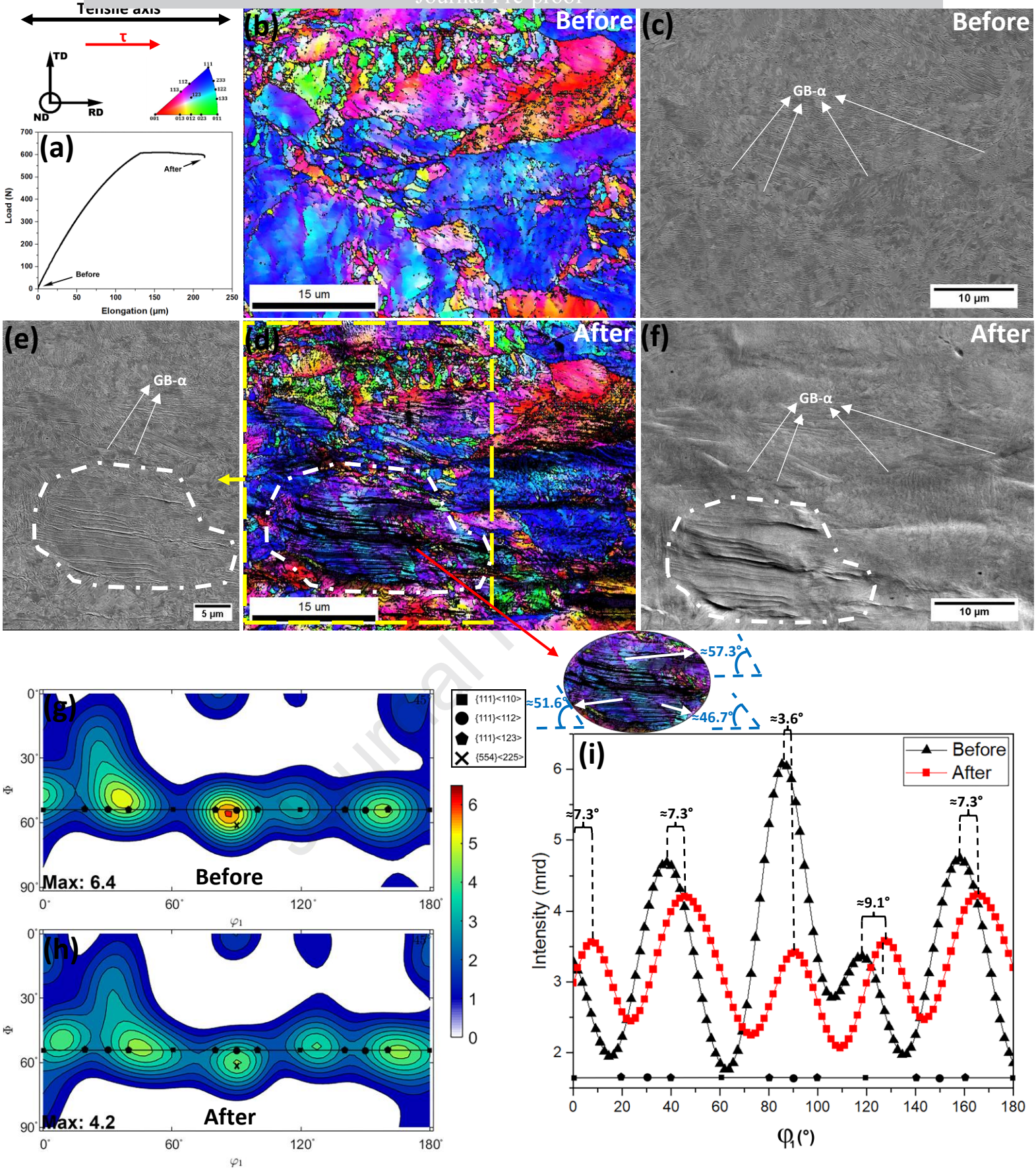

Figure 9. Interrupted shear-tensile experiment of deformed-refined (DR) specimen **(a)** Elongation-load curve of, **(b)** color-coded inverse pole figure (IPF) map before, **(c)** backscattered electron (BSE) image on the same area of the color-coded IPF map before, **(d)** color-coded IPF map after, **(e)** BSE image on the area indicated by a yellow dashed rectangle in the IPF map after, **(f)** SE image on the same area of the IPF map after, **(g)** orientation distribution function (ODF) at φ2 = 45° calculated with monoclinic symmetry from the IPF map before, and **(h)** ODF at φ2 = 45° calculated with monoclinic symmetry from the IPF map after the interrupted DR's tensile-shear experiment. **(i)** Intensity of the γ (ND//<111>) fiber in the ODFs shown in **Figures 9 (g)** and **(h)**.

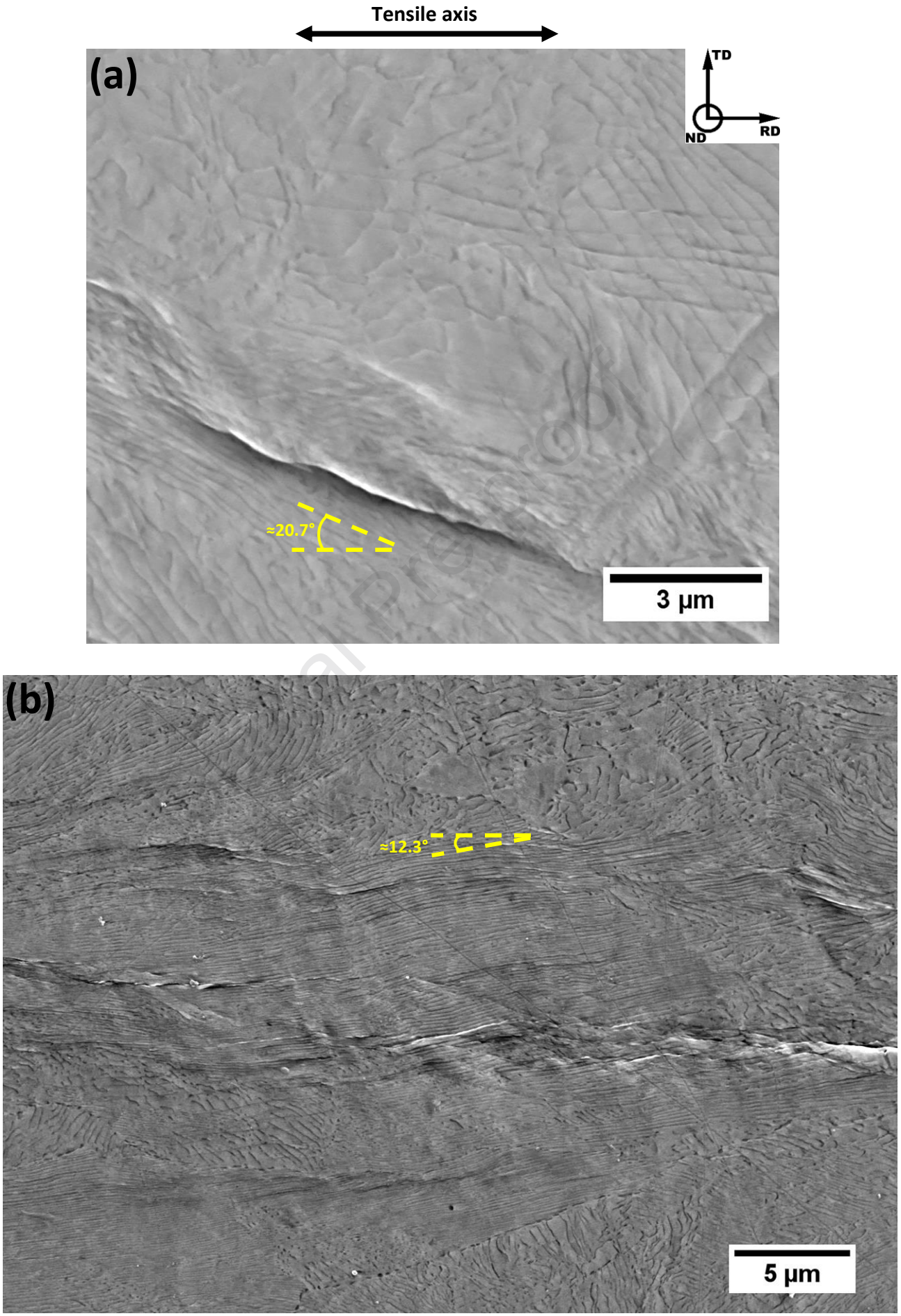

Figure 10. Secondary electron (SE) image of decohesion in the cementite/ferrite interface after the interrupted tensile-shear test in pearlites with their lamellar morphological angles of **(a)** ≈20.7° **(b)** ≈12.3° about the tensile axis.

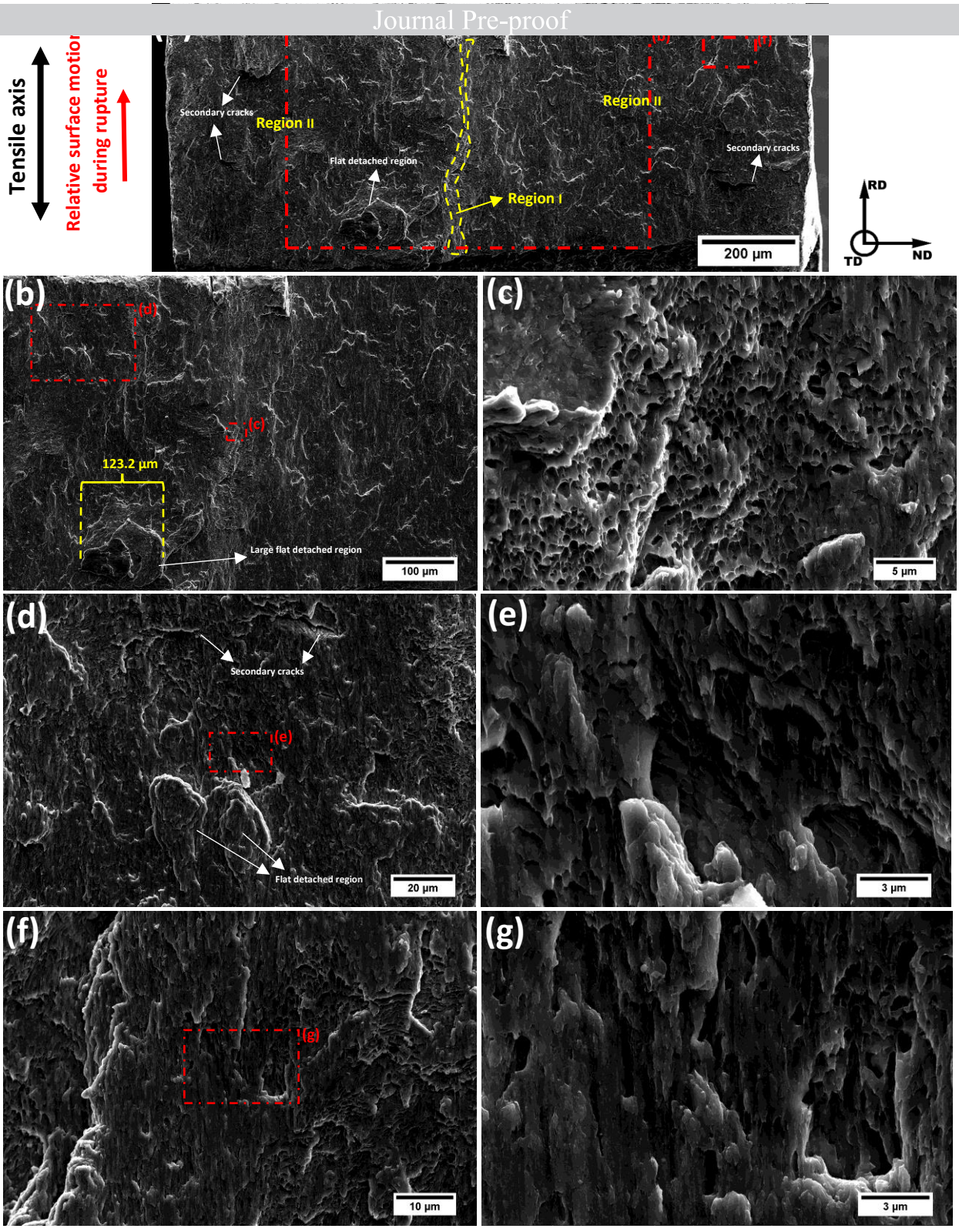

Figure 11. Scanning electron microscope (SEM) fractographic observation of the undeformed-coarse (UC) specimen after the in-situ tensile-shear test. **(a)** Overview of UC's shear fracture surface. **(b)** The central region of the UC's rupture surface. **(c)** Shear fracture with dimples (region I). **(d)(e)(f)(g)** Shear fracture with a flat surface (Region II).

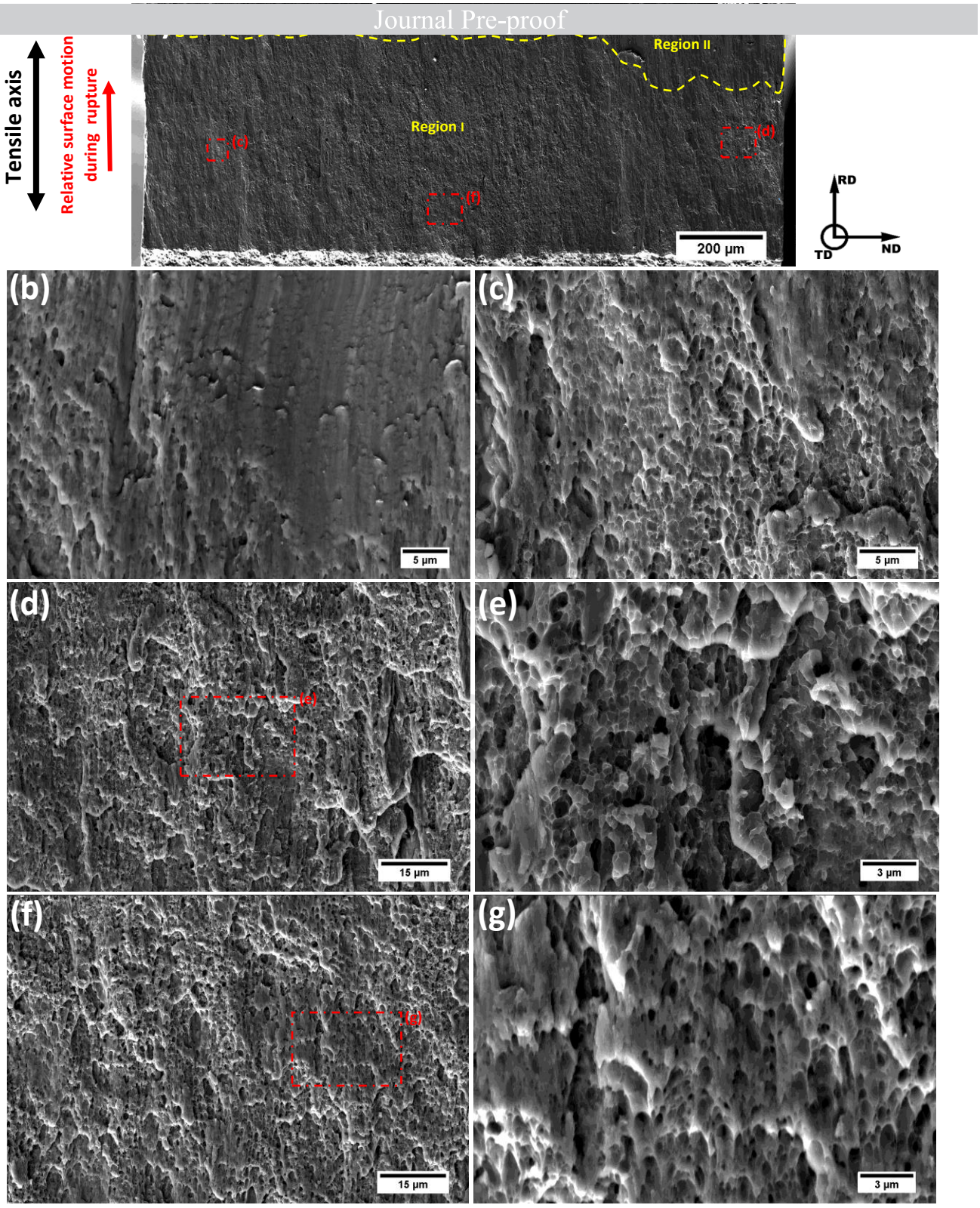

Figure 12. Scanning electron microscope (SEM) fractographic observation of the deformed-refined (DR) specimen after the in-situ tensile-shear test. **(a)** Overview of DR's shear fracture surface. **(b)** Shear fracture with a flat surface (Region ll). **(c) (d)(e)(f)(g)** Shear fracture with dimples (region l).

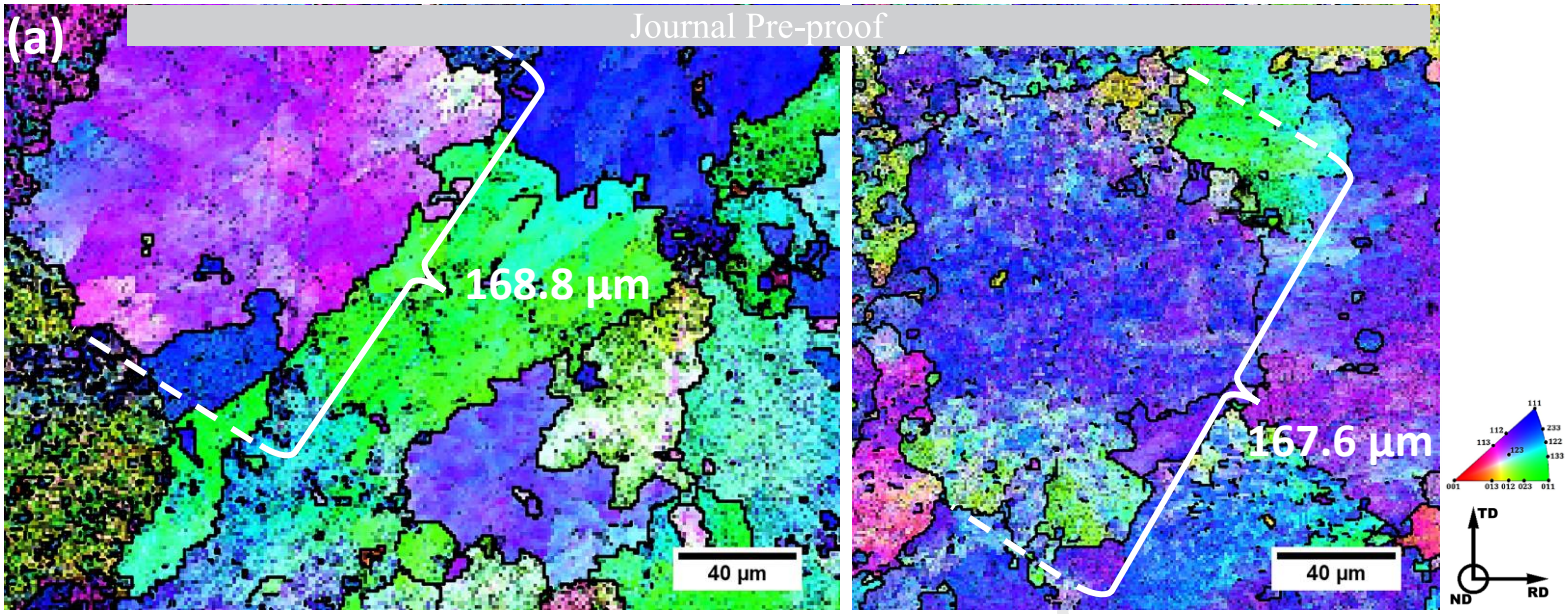

Figure 13. Color-coded inverse pole figure (IPF) maps on large areas of the non-deformed undeformed-coarse (UC) specimen containing their biggest pearlitic block size with the maximum length of **(a)** 168.8 µm, and **(b)** 167.6 µm.

Declaration of interests

☒ The authors declare that they have no known competing financial interests or personal relationships that could have appeared to influence the work reported in this paper.

☐The authors declare the following financial interests/personal relationships which may be considered as potential competing interests: